The Astrophysical Journal, 623:1115–1140, 2005 April 20

AN INFRARED SPECTROSCOPIC SEQUENCE OF M, L, AND T DWARFS[1]

Michael C. Cushing[2,3,4]
SETI Institute, NASA Ames Research Center, MS 245-3, Moffett Field, CA 94035; mcushing@arizona.edu

John T. Rayner
Institute for Astronomy, University of Hawaii, 2680 Woodlawn Drive, Honolulu, HI 96822; rayner@ifa.hawaii.edu

and

William D. Vacca[2]
SOFIA-USRA, NASA Ames Research Center, MS 144-2, Moffett Field, CA 94035; wvacca@mail.arc.nasa.gov
Received 2004 October 4; accepted 2004 December 13

ABSTRACT

We present a 0.6–4.1 μm spectroscopic sequence of M, L, and T dwarfs. The spectra have $R \equiv \lambda/\Delta\lambda \approx 2000$ from 0.9 to 2.4 μm and $R = 2500$–200 from 2.9 to 4.1 μm. These new data nearly double the number of L and T dwarfs that have reported L-band spectra. The near-infrared spectra are combined with previously published red-optical spectra to extend the wavelength coverage to $\sim$0.6 μm. Prominent atomic and molecular absorption features are identified including neutral lines of Al, Fe, Mg, Ca, Ti, Na, and K and 19 new weak CH_4 absorption features in the H-band spectra of mid- to late-type T dwarfs. In addition, we detect for the first time the 0–0 band of the $A\,^4\Pi$–$X\,^4\Sigma^-$ transition of VO at $\sim$1.06 μm in the spectra of L dwarfs and the P- and R-branches of the ν_3 band of CH_4 in the spectrum of a T dwarf. The equivalent widths of the refractory atomic features all decrease with increasing spectral type and are absent by a spectral type of $\sim$L0, except for the 1.189 μm Fe I line, which persists to at least $\sim$L3. We compute the bolometric luminosities of the dwarfs in our sample with measured parallaxes and find good agreement with previously published results that use L'-band photometry to account for the flux emitted from 2.5 to 3.6 μm. Finally, 2MASS J2224381−0158521 (L4.5) has an anomalously red spectrum and the strongest $\Delta\nu = +2$ CO bands in our sample. This may be indicative of unusually thick condensate clouds and/or low surface gravity.

Subject headings: infrared: stars — stars: fundamental parameters — stars: individual (2MASS J2224381−0158521) — stars: late-type — stars: low-mass, brown dwarfs

1. INTRODUCTION

Since the discovery of the first bona fide brown dwarfs (BDs; Basri et al. 1996; Rebolo et al. 1996; Nakajima et al. 1995), hundreds of very low-mass stars and BDs, collectively known as ultracool dwarfs, have been discovered in wide-field surveys such as the Two Micron All Sky Survey (2MASS; Skrutskie et al. 1997), the Deep Near Infrared Southern Sky Survey (DENIS; Epchtein et al. 1997), and the Sloan Digital Sky Survey (SDSS; York et al. 2000). The spectra of many of these ultracool dwarfs were sufficiently distinct from those of the latest M dwarfs that the creation of two new spectral types, "L" (Kirkpatrick et al. 1999b; Martín et al. 1999) and "T" (Burgasser 2001; Burgasser et al. 2002b), was warranted. The spectra of L dwarfs exhibit weak oxide bands (TiO and VO), strong hydride bands (FeH and CrH), and alkali lines (Na, K, Rb, and Cs) in the red optical and H_2O, FeH, and CO absorption bands in the near-infrared. The spectra of T dwarfs also show absorption due to alkali lines in the optical (although the Na and K lines are highly pressure broadened) but, in contrast to the L dwarfs, exhibit strong CH_4 bands along with H_2O bands and collision-induced absorption (CIA) due to H_2 in the near-infrared.

Since the spectral energy distributions of ultracool dwarfs peak in the near-infrared, it is advantageous to study them at these wavelengths. There have been numerous near-infrared spectroscopic studies of M, L, and T dwarfs (e.g., Jones et al. 1994; Ali et al. 1995; Leggett et al. 1996, 2001; Reid et al. 2001; Burgasser et al. 2000, 2002b), but the majority of the published spectra have low spectral resolving powers ($R \equiv \lambda/\Delta\lambda \lesssim 500$) and a range of signal-to-noise ratios (S/Ns). Although such spectra are suitable for studying variations in gross spectral morphology (e.g., defining spectral classification schemes; Reid et al. 2001; Geballe et al. 2002; Burgasser et al. 2002b), higher resolution spectra are required for more detailed analyses. For example, Saumon et al. (2000) analyzed an $R = 3000$ spectrum of Gl 229B (T6.5) to constrain its metallicity, while Cushing et al. (2003) identified nearly 100 new weak FeH absorption features in $R \approx 2000$ spectra of late-type M dwarfs and L dwarfs. McLean et al. (2003) have recently published a large sample of high-quality, moderate-resolution ($R = 2000$), near-infrared ($\sim$1–2.3 μm) spectra of late-type M, L, and T dwarfs, which greatly enhances the quality and number of ultracool dwarf spectra available for such analyses.

In contrast to the large number of published spectra covering from 1 to 2.5 μm, relatively little spectroscopic work on M, L, and T dwarfs has been done at $\lambda > 2.5$ μm, primarily because of the difficulty of observing from the ground at these

[1] Based in part on data collected at Subaru telescope, which is operated by the National Astronomical Observatory of Japan.
[2] Visiting Astronomer at the Infrared Telescope Facility, which is operated by the University of Hawaii under cooperative agreement NCC 5-538 with the National Aeronautics and Space Administration, Office of Space Science, Planetary Astronomy Program.
[3] Spitzer Fellow.
[4] Current address: Steward Observatory, 933 North Cherry Avenue, Tucson, AZ 85721.

TABLE 1
THE SAMPLE

Object (1)	Spectral Type (2)	J (mag) (3)	H (mag) (4)	K (mag) (5)	L' (mag) (6)	π (mas) (7)	π References (8)
Gl 229A	M1 V	4.98 ± 0.03	4.35 ± 0.03	4.15 ± 0.03	4.06 ± 0.05	173.19 ± 1.12	1
Gl 411	M2 V	4.10 ± 0.03	3.56 ± 0.03	3.36 ± 0.03	...	392.52 ± 0.91	1
Gl 388	M3 V	5.449 ± 0.027	4.843 ± 0.020	4.593 ± 0.017	...	204.6 ± 2.8	2
Gl 213	M4 V	7.124 ± 0.021	6.627 ± 0.018	6.389 ± 0.016	6.01 ± 0.05	172.75 ± 3.88	1
Gl 51	M5 V	8.611 ± 0.027	8.014 ± 0.023	7.718 ± 0.020	7.35 ± 0.06	95.5 ± 7.3	2
Gl 406	M6 V	7.085 ± 0.024	6.482 ± 0.042	6.084 ± 0.017	5.71 ± 0.05	419.1 ± 2.1	2
vB 8	M7 V	9.776 ± 0.029	9.201 ± 0.024	8.816 ± 0.023	...	154.5 ± 0.7	3
vB 10	M8 V	9.90 ± 0.03	9.24 ± 0.03	8.80 ± 0.03	8.18 ± 0.05	170.25 ± 1.37	1
LP 944−20	M9 V	10.725 ± 0.021	10.017 ± 0.021	9.548 ± 0.023	...	201.4 ± 4.2	4
LHS 2924	M9 V	11.990 ± 0.021	11.225 ± 0.029	10.744 ± 0.024	10.12 ± 0.03	92.4 ± 1.3	2
BRI 0021−0214	M9.5 V	11.992 ± 0.035	11.084 ± 0.022	10.539 ± 0.023	9.78 ± 0.13	86.6 ± 4.0	5
2MASS J07464256+2000321AB	L0.5	11.759 ± 0.020	11.007 ± 0.022	10.468 ± 0.022	9.67 ± 0.03	81.9 ± 0.3	4
2MASS J14392836+1929149	L1	12.759 ± 0.019	12.041 ± 0.019	11.546 ± 0.022	10.80 ± 0.05	69.6 ± 0.5	4
2MASS J02081833+2542533	L1	13.989 ± 0.026	13.107 ± 0.030	12.588 ± 0.027	...	...	
Kelu-1	L2	13.414 ± 0.026	12.392 ± 0.025	11.747 ± 0.023	10.78 ± 0.15	53.6 ± 2.0	4
2MASS J11463449+2230527AB	L3	14.165 ± 0.028	13.182 ± 0.026	12.590 ± 0.026	...	36.8 ± 0.8	4
2MASS J15065441+1321060	L3	13.365 ± 0.023	12.380 ± 0.021	11.741 ± 0.019	...	...	
2MASS J00361617+1821104	L3.5	12.466 ± 0.027	11.588 ± 0.029	11.058 ± 0.021	10.08 ± 0.05	114.2 ± 0.8	4
2MASS J22244381−0158521	L4.5	14.073 ± 0.027	12.818 ± 0.026	12.022 ± 0.023	10.90 ± 0.05	88.1 ± 0.1	4
2MASS J15074769−1627386	L5	12.830 ± 0.027	11.895 ± 0.024	11.312 ± 0.026	9.98 ± 0.03	136.4 ± 0.6	4
SDSS J053951.99−005902.0	L5	14.033 ± 0.031	13.104 ± 0.026	12.527 ± 0.024	11.32 ± 0.05	76.12 ± 2.17	6
2MASS J15150083+4847416	L6[a]	14.111 ± 0.029	13.099 ± 0.031	12.500 ± 0.024	...	...	
2MASS J08251968+2115521	L7.5	15.100 ± 0.034	13.792 ± 0.032	13.028 ± 0.026	11.53 ± 0.03	93.8 ± 1.0	4
DENIS-P J025503.3−470049.0	L8	13.246 ± 0.027	12.204 ± 0.024	11.558 ± 0.024	...	...	
SDSS J125453.90−012247.4	T2	14.891 ± 0.035	14.090 ± 0.025	13.837 ± 0.054	12.25 ± 0.05	84.9 ± 1.9	4
2MASS J05591915−1404489	T5	13.802 ± 0.024	13.679 ± 0.044	13.577 ± 0.052	12.14 ± 0.05	97.7 ± 1.3	4

NOTES.—J-, H-, and K-band photometry is from the 2MASS Point Source Catalog except for Gl 229A, Gl 411, and vB 10, which are from Leggett (1992) and on the CIT system. L'-band photometry is from Leggett et al. (1998, 2002) and Golimowski et al. (2004).

[a] Infrared spectral type.

REFERENCES.—(1) Perryman et al. 1997; (2) van Altena et al. 1995; (3) Monet et al. 1992; (4) Dahn et al. 2002; (5) Tinney et al. 1995; (6) Vrba et al. 2004.

wavelengths. Berriman & Reid (1987) were the first to detect H_2O absorption at ~ 3 μm in very low resolution ($R \approx 70$) spectra of early- to mid-type M dwarfs. Jones et al. (1995, 2002) used moderate-resolution spectra obtained from the ground and space to study this H_2O band in a small sample of M dwarf spectra. Even fewer spectra of L and T dwarfs at $\lambda > 2.5$ μm have been published. The ν_3 fundamental band of CH_4 at ~ 3.3 μm has been detected in the low-resolution spectra of two L dwarfs (Noll et al. 2000) and two T dwarfs (Oppenheimer et al. 1998; Burgasser 2001), while the fundamental CO band at 4.7 μm has been detected in the spectrum of Gl 229B (Noll et al. 1997). Recent observations from the *Spitzer Space Telescope* (Roellig et al. 2004) have also revealed H_2O, CH_4, and NH_3 absorption in the mid-infrared spectra of an L dwarf and a T dwarf. The paucity of M, L, and T dwarf spectra at these wavelengths is unfortunate since the H_2O, CH_4, CO, and NH_3 bands are useful probes of the atmospheric physics and chemistry of ultracool dwarfs (Saumon et al. 2003a, 2003b).

We have therefore undertaken a spectroscopic survey of M, L, and T dwarfs with the goal of creating a sample of high-S/N (>50), moderate-resolution ($R \approx 2000$) spectra covering a broad wavelength range (~ 0.9–4.1 μm). We present the first results of this survey in this paper. In § 2 we discuss the observations and data reduction. We describe the identification of prominent atomic and molecular absorption features and quantify the changes in the strengths of these features with spectral type in § 3. In § 4 we discuss two objects of interest: 2MASS J2224−0158 (L4.5), which exhibits an anomalously red near-infrared spectrum with deep CO bands, and DENIS J0255−4700, a late-type L dwarf (L8) that exhibits CH_4 absorption in both the H and K bands. In § 5 we compute the bolometric luminosities of the ultracool dwarfs in our sample. Finally, in § 6 we present a summary of our results.

2. OBSERVATIONS AND DATA REDUCTION

Our sample consists of 11 M dwarfs, 13 L dwarfs, and 2 T dwarfs. Table 1 lists the dwarfs' designations, spectral types, J-, H-, K-, and L'-band magnitudes, and parallaxes. Eight of the M dwarfs were selected from the list of primary spectral standards of Kirkpatrick et al. (1991); we have augmented this list with Gl 388 (AD Leo), LP 944−20, and BRI 0021−0214. The M dwarf spectral types are based on optical spectroscopy and are from Kirkpatrick et al. (1991, 1995, 1999b). The L and T dwarfs were drawn from the discoveries in 2MASS (Kirkpatrick et al. 1999b, 2000; Reid et al. 2000; Gizis et al. 2000; Burgasser et al. 2000; Wilson et al. 2003), DENIS (Martín et al. 1999), and SDSS (Leggett et al. 2000; Fan et al. 2000). We also included Kelu-1, which was discovered in a proper-motion survey (Ruiz et al. 1997). The L dwarf spectral types are based on optical spectroscopy and are from the L dwarf database maintained by J. D. Kirkpatrick.[5] The T dwarf spectral types are based on near-infrared spectroscopy and are from Burgasser et al. (2002b).

[5] Available at http://spider.ipac.caltech.edu/staff/davy/ARCHIVE.

TABLE 2
Log of SpeX Observations

Object (1)	Spectral Type (2)	UT Date (3)	Spectroscopy Mode (4)	R (5)	Exposure Time (s) (6)	A0 V Standard (7)
Gl 229A	M1 V	2002 Jan 10	SXD	2000	200	HD 42301
		2002 Jan 11	LXD2.1	2500	250	HD 42301
Gl 411	M2 V	2000 Dec 10	SXD	2000	60	HD 88960
		2000 Dec 10	LXD2.3	2500	500	HD 88960
Gl 388	M3 V	2000 Dec 10	SXD	2000	180	HD 88960
		2000 Dec 10	LXD2.3	1500	250	HD 88960
Gl 213	M4 V	2000 Dec 09	SXD	2000	720	HD 34203
		2000 Dec 09	LXD2.3	2500	500	HD 34203
Gl 51	M5 V	2000 Nov 06	SXD	2000	600	HD 5071
		2000 Nov 06	LXD2.3	1500	250	HD 11946
Gl 406	M6 V	2001 Jan 25	SXD	2000	360	HD 97585
		2001 Jan 24	LXD2.3	2500	500	HD 97585
vB 8	M7 V	2001 Jul 12	SXD	2000	1440	HD 148968
		2001 Jul 12	LXD1.9	938	660	HD 148968
vB 10	M8 V	2001 Jul 13	SXD	2000	1440	HD 183324
		2001 Jul 13	LXD1.9	938	600	HD 183324
LP 944−20	M9 V	2001 Jan 24	SXD	2000	1080	HD 18735
		2002 Jan 11	LXD1.9	938	2400	HD 183324
LHS 2924	M9 V	2003 Feb 23	SXD	2000	1200	HD 127304
		2003 Feb 24	LXD1.9	938	600	HD 127304
BRI 0021−0214	M9.5 V	2001 Oct 12	SXD	2000	1440	HD 9485
		2000 Nov 06	LXD1.9	938	720	HD 1663
2MASS J0746+2000AB	L0.5	2001 Jan 25	SXD	2000	1920	HD 64648
		2002 Feb 28	LXD1.9	938	1800	HD 64648
2MASS J1439+1929	L1	2001 Mar 22	SXD	2000	2160	HD 131951
		2003 Jul 06	LXD1.9	938	2280	HD 131951
2MASS J0208+2542	L1	2002 Nov 11	SXD	2000	2640	HD 13869
Kelu-1	L2	2001 Jan 25	SXD	2000	3120	HD 119752
		2001 Jan 24	LXD1.9	938	2460	HD 119752
		2002 Feb 28	LXD1.9	938	2280	HD 119752
2MASS J1146+2230AB	L3	2001 Mar 13	SXD	1200	3360	HD 105388
		2001 Mar 14	SXD	1200	4800	HD 105388
2MASS J1506+1321	L3	2001 Mar 13	SXD	2000	2640	HD 131951
		2002 Feb 28	LXD1.9	938	1800	HD 131951
2MASS J0036+1821	L3.5	2003 Aug 05	SXD	2000	1200	HD 6457
		2003 Aug 05	LXD1.9	938	1800	HD 6457
2MASS J2224−0158	L4.5	2001 Aug 07	SXD	2000	4320	HD 212404
2MASS J1507−1627	L5	2001 Mar 14	SXD	2000	2160	HD 133772
		2001 Mar 22	SXD	2000	2400	HD 133772
		2002 Feb 28	LXD1.9	938	1200	HD 124683
SDSS J0539−0059	L5	2001 Jan 24	SXD	1200	2400	HD 35656
2MASS J1515+4847	L6	2002 May 28	SXD	2000	4800	HD 116405
2MASS J0825+2115	L7.5	2001 Mar 12	SXD	1200	6960	HD 64648
		2001 Mar 13	SXD	1200	2880	HD 64648
		2001 Mar 14	SXD	1200	3120	HD 64648
DENIS J0255−4700	L8	2003 Sep 21	SXD	2000	1500	HD 21638
SDSS J1254−0122	T2	2001 Jan 25	SXD	1200	1920	HD 111744
		2001 Mar 13	SXD	1200	4080	HD 109309
2MASS J0559−1404	T5	2001 Jan 25	SXD	1200	2880	HD 41695

We obtained near-infrared spectra of the 26 dwarfs listed in Table 1 using two instruments: SpeX (Rayner et al. 2003), mounted on the 3.0 m NASA Infrared Telescope Facility (IRTF), and the Infrared Camera and Spectrograph (IRCS; Kobayashi et al. 2000), mounted on the 8.2 m Subaru telescope. SpeX was used for the majority of the observations, while the IRCS was used to obtain L-band spectra for the faintest targets. The following three subsections describe the acquisition and reduction of the data, the absolute flux calibration of the spectra, and the merging of the SpeX, IRCS, and published red-optical spectra to produce absolutely flux-calibrated 0.6–4.1 μm spectra.

2.1. *SpeX Observations*

SpeX is a 0.8–5.5 μm, medium-resolution, cross-dispersed spectrograph equipped with a 1024×1024 Aladdin 3 InSb array (Rayner et al. 2003). The entire 0.8–5.5 μm wavelength range can be covered at $R \approx 2000$ with two cross-dispersed modes. The SXD mode provides simultaneous coverage of the 0.8–2.4 μm wavelength range, except for a 0.06 μm gap between the H and K bands, while the LXD1.9, LXD2.1, and LXD2.3 modes cover the 1.9–4.2, 2.1–5.0, and 2.3–5.5 μm wavelength ranges, respectively. The length of the slit in all of these modes is 15″.

The observations were conducted over a period of 3 yr beginning with SpeX commissioning in 2000 May and ending in 2003 October. A log of the observations, including the UT date of observation, spectroscopic mode, resolving power, total on-source integration time, and associated telluric standard star, is given in Table 2. The 0.″3 and 0.″5 slits were used in the SXD mode and provide a resolving power of 2000 and 1200, respectively. Three slits with widths of 0.″3, 0.″5, and 0.″8, corresponding to a resolving power of 2500, 1515, and 938, respectively, were used in the LXD modes.

To facilitate subtraction of the additive components of the total signal (electronic bias level, dark current, sky and background emission), the observations were obtained in a series of exposures in which the target was placed at two different positions along the slit separated by 7.″8. An A0 V star was observed before or after each target to correct for absorption due to the Earth's atmosphere and to flux-calibrate the science object spectra. The air-mass difference between the object and "telluric standard" was almost always less than 0.1 and usually less than 0.05. However, in a few cases in which there was a paucity of nearby A0 V stars, the air-mass difference was as large as 0.2. Finally, a series of flat-field exposures and argon arc lamp exposures were taken after each object/standard pair for flat-fielding and wavelength calibration purposes.

We reduced the data using Spextool (Cushing et al. 2004), the facility IDL-based data reduction package for SpeX. The initial image processing consisted of correcting each science frame for nonlinearity, subtracting the pairs of images taken at the two different slit positions, and dividing the pair-subtracted images by a normalized flat field. The spectra were then optimally extracted and wavelength calibrated. All wavelengths are given in vacuum. The dwarf spectra were corrected for telluric absorption and flux-calibrated (to roughly $\pm$10%) using the extracted A0 V spectra and the technique described by Vacca et al. (2003). For each cross-dispersed mode, the spectra from different orders were merged together to form a continuous spectrum. In principle, the flux density levels of the spectra in two overlapping orders should match exactly, but in practice we find mismatches of up to 3% but typically less than 1%. Any mismatch was removed by scaling one spectrum to the level of the other. The combined spectra were then smoothed with a Savitzky-Golay kernel (Press et al. 1992). Each LXD spectrum was scaled to match the flux density level of the corresponding SXD spectrum, and then the two spectra were combined.

Although the spectra in adjacent orders are scaled to a common flux density level during the merging process, errors can be introduced in the relative flux density levels of the spectra if the S/N in the overlap regions, which is used to determined the scaling factor, is low. Such is the case for dwarf stars with spectral types $\gtrsim$M6 because of the strong intrinsic water absorption bands present at the wavelengths of the order overlaps. Therefore, we computed synthetic $J-H$, $H-K$, and $K-L'$ colors of the dwarfs from our sample and compared them with the colors derived from the published photometry presented in Table 1 to determine if any errors were introduced during the merging process.

The synthetic color for two bandpasses X and Y is given by

$$X - Y = -2.5 \log \left[\frac{\int \lambda f_\lambda^{\rm obj}(\lambda) T_X(\lambda)\, d\lambda}{\int \lambda f_\lambda^{\rm Vega}(\lambda) T_X(\lambda)\, d\lambda} \right] + 2.5 \log \left[\frac{\int \lambda f_\lambda^{\rm obj}(\lambda) T_Y(\lambda)\, d\lambda}{\int \lambda f_\lambda^{\rm Vega}(\lambda) T_Y(\lambda)\, d\lambda} \right], \quad (1)$$

TABLE 3
Dwarf Color Residuals

Parameter	Value
$\langle \delta_{J-H} \rangle$	$+0.00 \pm 0.04$
$\langle \delta_{H-K} \rangle$	$+0.02 \pm 0.03$
$\langle \delta_{K-L'} \rangle$	-0.01 ± 0.07

Notes.—Here $\delta_{X-Y} = (X-Y)_{\rm obs} - (X-Y)_{\rm syn}$. The errors are given by the rms deviation.

where $f_\lambda^{\rm Vega}(\lambda)$ is the flux density of Vega, $f_\lambda^{\rm obj}(\lambda)$ is the flux density of the object, and $T(\lambda)$ is the transmission function for each bandpass, which we assume to be given by the product of the filter transmission and the typical atmospheric transmission at an air mass of 1 for the site at which the observation was conducted. For $f_\lambda^{\rm Vega}(\lambda)$ we used a Kurucz model of Vega ($T_{\rm eff} = 9550$ K, $\log g = 3.950$, $v_{\rm rot} = 25$ km s^{-1}, and $v_{\rm turb} = 2$ km s^{-1}), scaled to the flux density at $\lambda = 5556$ Å given by Mégessier (1995). Equation (1) assumes that Vega has a color of zero. The factors of λ inside the integrals convert the energy flux densities f_λ to photon flux densities, which ensures that the integrated fluxes are proportional to the observed photon count rate (e.g., Koornneef et al. 1986; Buser & Kurucz 1992). The California Institute of Technology (CIT) *JHK* and Mauna Kea Observatories Near-Infrared (MKO-NIR) L' transmission functions were kindly provided by S. Leggett (2002, 2003, private communication), while the 2MASS filter transmissions are from Cohen et al. (2003).[6] We computed the residuals [$\delta_{X-Y} = (X-Y)_{\rm obs} - (X-Y)_{\rm syn}$] between the observed and synthetic $J-H$, $H-K$, and $K-L'$ colors of each dwarf. The average residuals are given in Table 3 and indicate that no significant errors were introduced in the relative flux density levels of spectra in adjacent orders during the order merging process.

The final step in the reduction process was to absolutely flux-calibrate the spectra using the published photometry listed in Table 1. For each spectrum, we computed correction factors given by

$$C_X = 10^{-0.4 m_X} \frac{\int \lambda f_\lambda^{\rm Vega}(\lambda) T_X(\lambda)\, d\lambda}{\int \lambda f_\lambda^{\rm obs}(\lambda) T_X(\lambda)\, d\lambda}, \quad (2)$$

where m_X is the magnitude of the object in the J, H, and K bands and the remaining variables have the same meaning as in equation (1). The errors in the correction factors were computed using the errors in the published magnitudes. Each spectrum was then multiplied by the weighted average of the J-, H-, and K-band correction factors. The average correction factors ranged from 0.9 to 1.05 with a median value of 0.92.

2.2. *IRCS Observations*

The IRCS is a facility infrared imager and spectrograph for the 8.2 m Subaru telescope. The imager, which is equipped with a 1024×1024 Alladin 3 InSb array, also contains grisms for low-resolution spectroscopy. We used the L-band grism (2.90–4.16 μm) with slit widths of 0.″3 and 0.″6 to achieve spectral resolving powers of $\sim$425 and $\sim$212, respectively.

A log of the observations, including the UT date of observation, the resolving power R, total on-source integration time,

[6] Note that the λ factors should be removed from eq. (1) when using the 2MASS filter transmission curves from Cohen et al. (2003) because the curves have already been multiplied by λ.

TABLE 4
Log of IRCS Observations

Object (1)	Spectral Type (2)	UT Date (3)	R (4)	Exposure Time (s) (5)	A0 V Standard (6)
2MASS J2224−0158	L4.5	2002 Dec 12	425	560	HD 215143
SDSS J0539−0059	L5	2002 Dec 09	425	600	HD 37887
2MASS J0825+2115	L7.5	2001 May 06	212	1800	HD 64648
DENIS J0255−4700	L8	2002 Dec 09	212	252	HD 28813
SDSS J1254−0122	T2	2001 May 06	212	1800	HD 109309
2MASS J0559−1404	T5	2002 Dec 09	212	2590	HD 47596

and A0 V telluric standard star, is given in Table 4. The observing strategy was identical to that employed in the SpeX observations. A series of exposures were taken in pairs with the targets at two different positions separated by 5″ along the 20″ long slit. A nearby A0 V star was also observed for each science object to correct for absorption due to the Earth's atmosphere, and a series of flat-field exposures and dark frames were taken at the end of each night.

The spectra were extracted using a modified version of Spextool (Cushing et al. 2004). Each pair of target exposures was subtracted and then flat-fielded. The spectra were then extracted and wavelength calibrated using sky emission features. The telluric correction process is much simpler than in the case of the SpeX observations because at these wavelengths, the continuum of the A0 V standard star is well approximated by a blackbody and the hydrogen lines are relatively weak. Therefore, we divided the object spectrum by the standard-star spectrum to remove the telluric absorption and instrument throughput and then multiplied the result by a Planck function of 9500 K, the effective temperature of A0 V stars (Tokunaga 2000), to restore the continuum shape of the object.

The IRCS spectra must be absolutely flux-calibrated using L'-band photometry before they can be combined with the SpeX spectra since the two sets of spectra do not overlap in wavelength. DENIS J0255−4700 lacks a published L' magnitude so we observed it at L' using the SpeX guider camera on 2003 October 03 UT and measured $m_{L'} = 10.2 \pm 0.1$. After the IRCS spectra are flux-calibrated using the L'-band photometry, they were merged with the SpeX spectra.

2.3. *Combining the Optical and Infrared Spectra*

The near-infrared spectra were extended blueward to ∼0.6 μm using published red-optical spectra. These spectra, which cover from roughly 0.6 to 0.95 μm and typically have resolutions ranging from 9 to 18 Å ($R = 890$–444), are from Kirkpatrick et al. (1991, 1999b, 2000), Tinney & Reid (1998), Martín et al. (1999), Fan et al. (2000), Gizis et al. (2000), Reid et al. (2000), Burgasser et al. (2003), and T. Henry (2004, private communication). For each dwarf, the wavelengths of the optical spectrum were converted from air to vacuum if necessary. The optical spectrum was scaled to the same flux level as the flux-calibrated SpeX spectrum and linearly interpolated onto the wavelength grid of the SpeX spectrum. The two spectra were then combined using a mean. Since many of the optical spectra have not been corrected for telluric absorption, care was taken to scale the spectra using wavelength ranges with a minimal amount of telluric absorption, namely, 0.81–0.83 μm and 0.99–1.05 μm.

Figure 1 shows a subset of the flux-calibrated 0.6–4.1 μm spectra of the dwarfs listed in Table 1. The S/N of the spectra in the J, H, and K bands ranges from ∼50 in the T dwarfs to ∼200 in the M dwarfs. The S/N in the L' band is typically lower, ranging from ∼10 in the T dwarfs to ∼100 in the M dwarfs.

3. ANALYSIS

3.1. *Feature Identifications*

The identification of atomic and molecular absorption features in the spectra of M, L, and T dwarfs is important because they can be used to constrain the effective temperatures ($T_{\rm eff}$), surface gravities ($\log g$), and metallicities ([M/H]) of the dwarfs. In addition, the process allows the identification of opacity sources not currently included in atmospheric models. There have been numerous infrared spectroscopic studies that identify both atomic and molecular absorption features in the spectra of M, L, and T dwarfs (e.g., Jones et al. 1994; Ali et al. 1995; Leggett et al. 1996; McLean et al. 2000; Reid et al. 2001; Burgasser et al. 2000, 2002b). However, the quality of the identifications ranges from secure to questionable because, in some cases, the spectra have low spectral resolution, low S/N, small wavelength coverage, and/or sparse spectral type coverage. Since our data do not suffer from these shortcomings, we have conducted a systematic search for both atomic and molecular features in our M, L, and T dwarf spectra. We have confined our search to $\lambda \gtrsim 0.95$ μm since Kirkpatrick et al. (1991, 1995, 1999b) have adequately identified the atomic and molecular features in the spectra of ultracool dwarfs shortward of this wavelength.

We describe the identification of the molecular and atomic features in the following two subsections. Many of the features are weak and could easily be mistaken for noise. However, we are confident in our identifications because the features can be tracked through the spectral sequence. Table 5 lists the identified molecular features, while Table 6 lists the identified atomic features. Finally, we avoid the use of the term "lines" since at $R \approx 2000$ many of the features, especially the molecular ones, are blends of many individual lines.

3.1.1. *Molecular Features*

TiO.—Absorption bands of TiO that arise from the γ ($A\,^3\Phi$–$X\,^3\Delta$), γ' ($B\,^3\Pi$–$X\,^3\Delta$), δ ($b\,^1\Pi$–$a\,^1\Delta$), and ϵ ($E\,^3\Pi$–$X\,^3\Delta$) systems are prominent in the red-optical spectra of mid- to late-type M stars (e.g., Kirkpatrick et al. 1991; Tinney & Reid 1998) and early-type L dwarfs (Kirkpatrick et al. 1999b). The ϕ ($b\,^1\Pi$–$d\,^1\Sigma$) system has also been detected in the spectra of giant stars (Joyce et al. 1998) but never, to our knowledge, in the spectra of field dwarf stars.[7] However, synthetic spectra of M dwarfs computed from the model atmospheres of Allard et al. (2000) predict a strong 0–0 band head at ∼1.104 μm.

[7] The ϕ band of TiO has been detected in the spectrum of the young brown dwarf KPNO Tau 4 by McGovern et al. (2004).

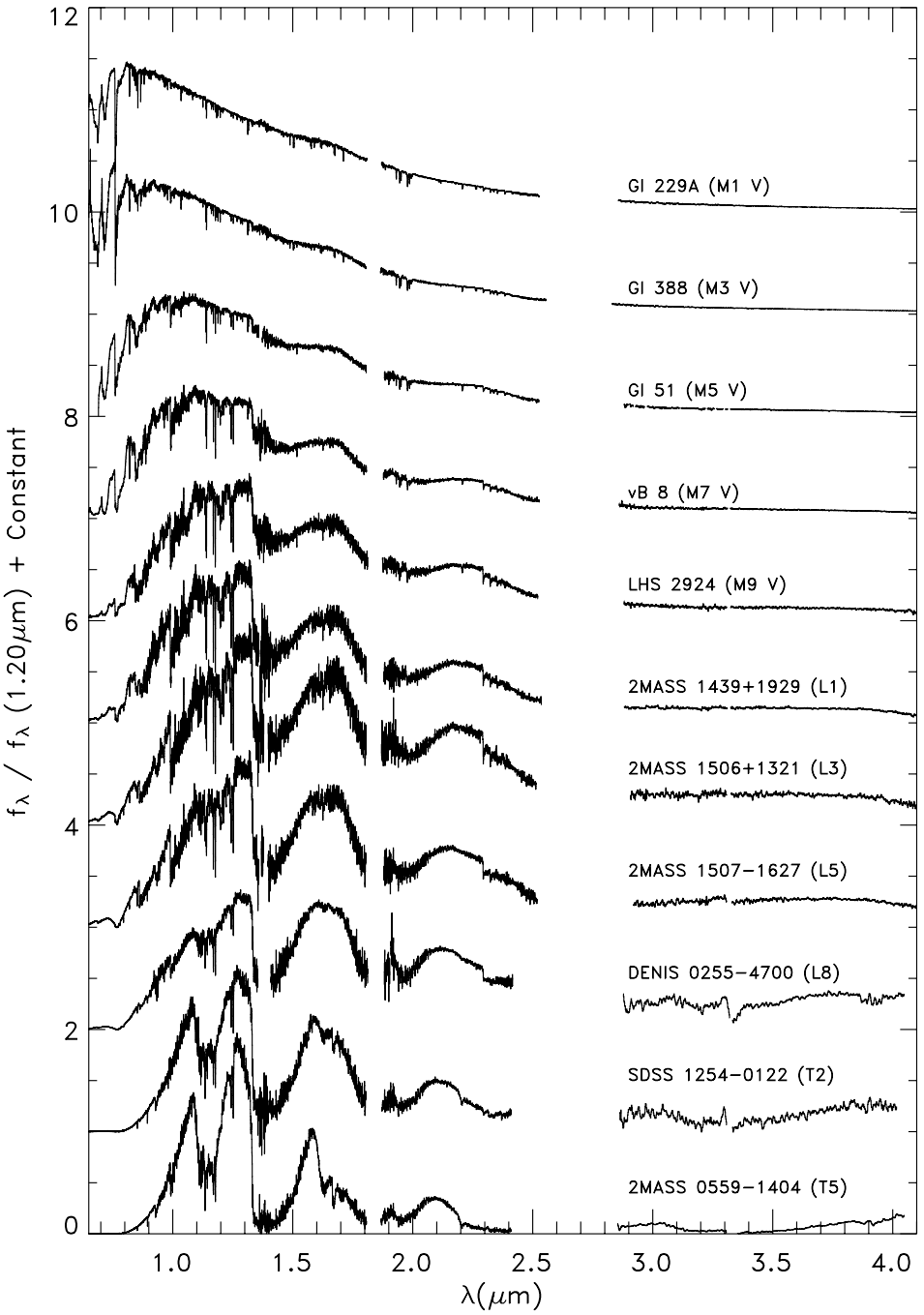

FIG. 1.—The 0.6–4.1 μm sequence of M, L, and T dwarfs. The gaps in the spectra at $\sim$1.85 μm are due to a break in the wavelength coverage of the SXD mode of SpeX. The spectra from 2.5 to 2.9 μm were removed because the atmosphere is opaque at these wavelengths.

We have compared the high-resolution ($R = 800{,}000$) Fourier Transform Spectrometer (FTS) emission spectrum[8] of TiO used in the analysis of the ϕ system by Galehouse et al. (1980) to our M and L dwarf spectra in order to determine to what extent the 0–0 band of the ϕ system is present. We smoothed the TiO spectrum to $R = 2000$ and then resampled it onto the wavelength grid of the dwarfs. We find no evidence of absorption due to the 0–0 band in the spectra of the M and L dwarfs.

VO.—Absorption bands of VO arising from the $B\,^4\Pi$–$X\,^4\Sigma^-$ system are prominent in the red-optical spectra of late-type M dwarfs (Kirkpatrick et al. 1991, 1995; Tinney & Reid 1998). The $A\,^4\Pi$–$X\,^4\Sigma^-$ system produces three bands, the 1–0 at $\sim$0.96 μm, the 0–0 at $\sim$1.06 μm, and the 0–1 at 1.18 μm. The 0–0 and 0–1 bands and their associated band heads have been detected in the spectra of M giants (e.g., Joyce et al. 1998); the 1–0 band is difficult to detect because of contamination by telluric H_2O absorption. Kirkpatrick et al. (1993) identified the 0–0 band in the spectrum of vB 8 (M7 V), and Kirkpatrick et al. (1999a) claimed to detect this band in the spectrum of GD 165 B (L4). However, the Kirkpatrick et al. (1999a) spectrum of GD 165 B is missing the wavelengths centered on the 0–0 band of VO, which casts doubt on the identification.

We have compared our spectrum of vB 10 (M8 V) with a high-resolution FTS emission spectrum of VO kindly provided by S. Davis (2002, private communication) in order to confirm

[8] We obtained the spectrum (770629R0.005) using the National Solar Observatory Digital Library Query Tool, http://diglib.nso.edu/nso_user.html.

TABLE 5

MOLECULAR FEATURES IN DWARF SPECTRA

Wavelength (μm) (1)	Species (2)	Transition (3)	References (4)
0.89–0.99	H_2O	$3\nu_3$, $\nu_1+2\nu_3$, $2\nu_1+\nu_3$, $3\nu_1$, $\nu_1+2\nu_2+\nu_3$, $2\nu_1+2\nu_2$	1
0.9896 head	FeH	0–0 band of $F\ ^4\Delta$–$X\ ^4\Delta$	2
1.00606 Q-branch	FeH	0–0 band of $F\ ^4\Delta$–$X\ ^4\Delta$	3
1.05–1.08	VO	0–0 band of $A\ ^4\Pi$–$X\ ^4\Sigma^-$	4
1.09–1.20	H_2O	$\nu_2+2\nu_3$, $\nu_1+\nu_2+\nu_3$, $2\nu_1+\nu_2$, $3\nu_2+\nu_3$, $\nu_1+2\nu_2$	1
1.1–1.24	CH_4	$3\nu_3$	5
1.1939 head	FeH	0–1 band of $F\ ^4\Delta$–$X\ ^4\Delta$	2
1.22210 Q-branch	FeH	0–0 band of $F\ ^4\Delta$–$X\ ^4\Delta$	3
1.2389 head	FeH	1–2 band of $F\ ^4\Delta$–$X\ ^4\Delta$	2
1.3–1.51	H_2O	$2\nu_3$, $\nu_1+\nu_2$, $2\nu_1$, $2\nu_2+\nu_3$, $\nu_1+2\nu_2$	1
1.58263 head	FeH	0–0 band of $E\ ^4\Pi$–$A\ ^4\Pi$	6
1.59188 head	FeH	0–0 band of $E\ ^4\Pi$–$A\ ^4\Pi$	6
1.62457 head	FeH	0–0 band of $E\ ^4\Pi$–$A\ ^4\Pi$	6
1.6–1.8	CH_4	$2\nu_3$, $2\nu_2+\nu_3$	7
1.75–2.05	H_2O	$\nu_2+\nu_3$, $\nu_1+\nu_2$, $3\nu_2$	1
2.3–3.2	H_2O	ν_1, ν_3, $2\nu_2$	1
2.15–2.5	CH_4	$\nu_3+\nu_4$, $\nu_2+\nu_3$	7
2.29352 head	^{12}CO	2–0 band of $X\ ^1\Sigma^+$–$X\ ^1\Sigma^+$	8
2.32266 head	^{12}CO	3–1 band of $X\ ^1\Sigma^+$–$X\ ^1\Sigma^+$	8
2.34483 head	^{13}CO	2–0 band of $X\ ^1\Sigma^+$–$X\ ^1\Sigma^+$	8
2.35246 head	^{12}CO	4–2 band of $X\ ^1\Sigma^+$–$X\ ^1\Sigma^+$	8
2.38295 head	^{12}CO	5–3 band of $X\ ^1\Sigma^+$–$X\ ^1\Sigma^+$	8
2.41414 head	^{12}CO	6–4 band of $X\ ^1\Sigma^+$–$X\ ^1\Sigma^+$	8
1.8–2.8	H_2	1–0 quadrupole (CIA)	9
3.4–4.2 heads	OH	$\Delta\nu=+1$, +2 band heads	10
3.0–3.8	CH_4	ν_3	11

REFERENCES.—(1) Auman 1967; (2) Phillips et al. 1987; (3) Cushing et al. 2003; (4) Chueng et al. 1982; (5) Danielson 1966; (6) Wallace & Hinkle 2001; (7) Leggett et al. 2000; (8) Goorvitch 1994; (9) Borysow et al. 1997; (10) Wallace & Hinkle 2002; (11) Noll et al. 2000.

TABLE 6

ATOMIC FEATURES IN DWARF SPECTRA

Vacuum λ (μm)	Elements	Vacuum λ (μm)	Elements	Vacuum λ (μm)	Elements	Vacuum λ (μm)	Elements
0.95500460	Ti I	1.0608472	Si I, Ti I	1.2528860	K I	1.9781980	Ca I
0.96042912	Ti I	1.0664966	Ti I, Si I	1.2682125	Na I	1.9817054	Ca I
0.96408301	Ti I	1.0697268	Si I	1.2827300	H I, Ti I	1.9865941	Ca I
0.96516997	Ti I	1.1258730	Al I	1.2851494	Ti I	1.9930196	Ca I
0.96774343	Ti I	1.1383850	Na I	1.2883723	Fe I	1.9968176	Ca I
0.96923371	Ti I	1.1408517	Na I	1.2904632	Mn I	2.1066365	Mg I
0.97085682	Ti I	1.1593413	Fe I	1.2982085	Mn I	2.1098654	Al I
0.97315592	Ti I	1.1612996	Fe I	1.3130514	Al I	2.1168456	Al I, Si I
0.97465017	Ti I	1.1640519	Fe I	1.4878380	Mg I	2.1789074	Si I, Ti I
0.97708032	Ti I	1.1692427	K I, Fe I	1.5028185	Mg I	2.2062996	Na I
0.97884568	Ti I	1.1778406	K I	1.5046375	Mg I	2.2089866	Na I
0.98357543	Ti I	1.1801096	Fe I	1.5167645	K I	2.2215927	Ti I
1.0219217	Fe I	1.1833522	Mg I	1.5753070	Mg I	2.2237389	Ti I
1.0328393	Sr II	1.1891897	Fe I	1.5771145	Mg I	2.2275054	Fe I, Ti I
1.0347329	Fe I, Ca I	1.1974243	Fe I, Ti I	1.5894133	Si I	2.2317958	Ti I
1.0382309	Si I	1.1995492	Si I	1.6723852	Al I	2.2390381	Fe I
1.0399835	Fe I, Ti I	1.2035899	Si I	1.6755865	Al I	2.2626701	Ca I
1.0426753	Fe I	1.2086007	Mg I	1.7110102	Mg I	2.2656055	Ca I
1.0471180	Fe I	1.2111957	Si I	1.9314969	Ca I	2.2819887	Mg I
1.0500833	Ti I	1.2273618	Si I	1.9458160	Ca I	2.3354050	Na I
1.0588292	Ti I, Si I	1.2436839	K I	1.9509361	Ca I	2.3383542	Na I

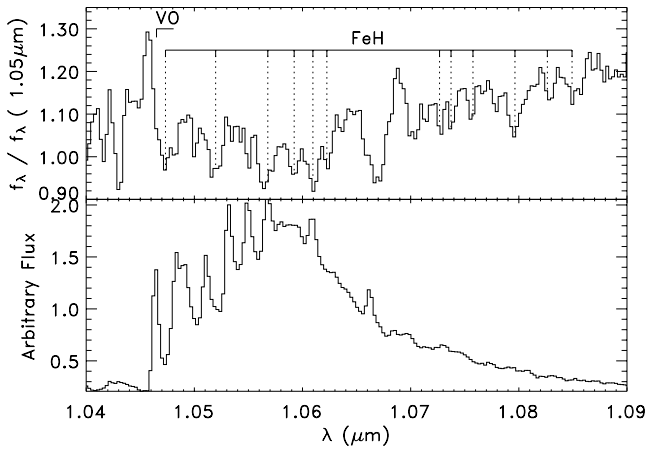

FIG. 2.—*Bottom*: VO emission spectrum. *Top*: Spectrum of vB 10 (M8 V). FeH features previously identified are indicated by dotted lines. The broad absorption feature in the spectrum of vB 10 is due to VO.

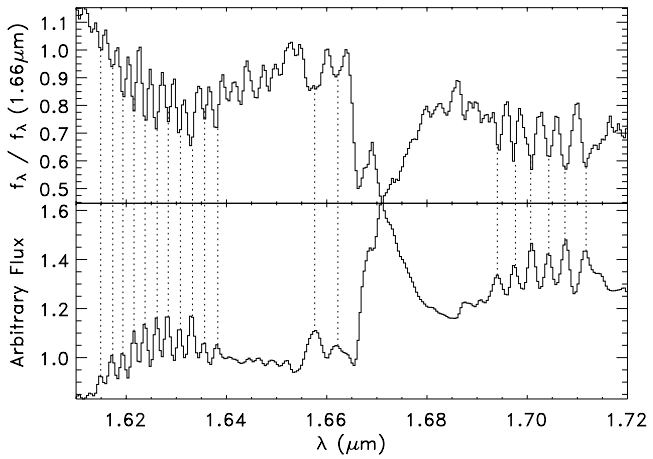

FIG. 4.—*Bottom*: CH_4 emission spectrum. *Top*: Spectrum of 2MASS J0559−1404 (T5) centered on the $2\nu_3$ band. The positions of the 19 features common to both spectra are indicated by dotted lines.

the presence of the 0–0 band of VO in the spectra of M and L dwarfs. The FTS spectrum was smoothed to $R = 2000$ and then resampled onto the wavelength grid of vB 10. Figure 2 shows the spectrum of vB 10 in the top panel and the emission spectrum of VO in the bottom panel. It is apparent that the broad feature in the vB 10 spectra centered at 1.06 μm is due to the 0–0 band of VO. However, almost all of the high-frequency features seen in the vB 10 spectrum have been ascribed to FeH (Cushing et al. 2003). It may be that some of the features in this wavelength range identified as FeH are actually a blend of both FeH and VO lines.

In order to quantify the variation of the strength of this band as a function of spectral type, we followed Kirkpatrick et al. (1995) and defined a spectral index that measures the ratio of the flux density in the band to the expected flux density at the same wavelength based on a linear interpolation between continuum points on either side of the band. This index is given by

$$z\text{-VO} = \frac{0.4667 f_{1.084} + 0.5334 f_{1.039}}{f_{1.06}}, \qquad (3)$$

where f_{λ_0} is the mean flux density in a 0.008 μm window centered around λ_0. Larger values of z-VO imply deeper absorption. The VO indices computed for the dwarfs in our sample are shown as a function of spectral types in Figure 3. The error bars

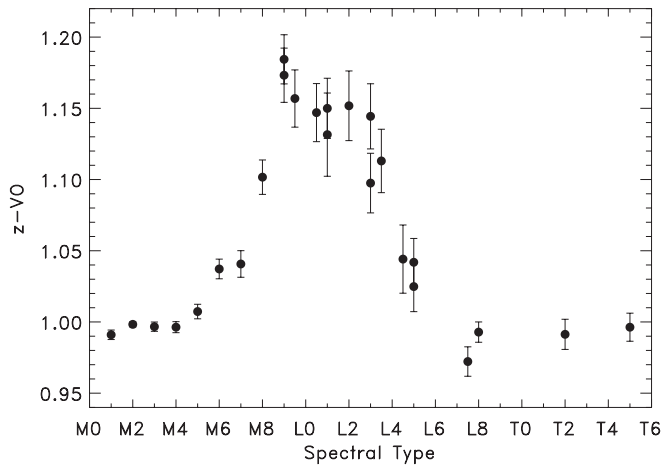

FIG. 3.—The z-VO index as a function of spectral type.

were computed from the uncertainties in the mean flux densities in $f_{1.039}$, $f_{1.06}$, and $f_{1.084}$. The VO band first appears at a spectral type of ∼M6, peaks in strength at ∼L0, and disappears by ∼L5. The strengths of the 1–0 and 0–0 bands of the $B\ ^4\Pi$–$X\ ^4\Sigma^-$ system peak at ∼M9 (Kirkpatrick et al. 1999b), which lends further credence to the idea that the broad feature at 1.06 μm is carried by VO. Given that the Kirkpatrick et al. (1999a) GD 165B spectrum is missing the wavelengths centered on this band, this is the first detection of the 0–0 band of the $A\ ^4\Pi$–$X\ ^4\Sigma^-$ transition of VO in the spectra of L dwarfs.

CrH.—The appearance of the CrH band head, which arises from the 0–0 band of the $A\ ^6\Sigma^+$–$X\ ^6\Sigma^+$ system, at 0.8611 μm in the spectra of late-type dwarfs is one of the defining characteristics of the L spectral class (Kirkpatrick et al. 1999b; Martín et al. 1999). Although the 0–1 band head of the same system at ∼0.9969 μm is also often identified in the spectra of late-type dwarfs, Cushing et al. (2003) have shown that in $R = 2000$ spectra many of the absorption features near this wavelength can be attributed to the 0–0 band of the $F\ ^4\Delta$–$X\ ^4\Delta$ system of FeH. As a result, the extent to which the 0–1 band is present in the spectra of late-type dwarfs remains uncertain until higher resolution spectra can be obtained.

Burrows et al. (2002) have computed new line lists and opacities for 12 bands of the $A\ ^6\Sigma^+$–$X\ ^6\Sigma^+$ system of CrH. In addition to the 0–0 and 0–1 bands, this system also has bands in the near-infrared at ∼1.18 (0–2) and ∼1.4 μm (0–3). The 0–3 band will be difficult to identify because it falls within the strong water absorption band, both telluric and intrinsic to the dwarfs, centered at the same wavelength. In order to determine the extent to which the 0–2 band is present in the spectra of L dwarfs, we have compared the CrH cross section spectrum of Burrows et al. (2002) with the J-band spectrum of 2MASS J1507−1627 (L5). We chose an L5 dwarf to maximize our chances of identifying any CrH features since the strength of the 0–0 band at 0.8611 μm peaks at this spectral type (Kirkpatrick et al. 1999b). Nevertheless, we find no evidence of CrH absorption features in the J-band spectrum of 2MASS J1507−1627. Burgasser et al. (2003) noted that the weakness of the CrH band at 0.9969 μm in L dwarf spectra is probably due to the low CrH/FeH equilibrium abundance ratio of $\sim 10^{-3}$ for 1800 K $\leq T_{\rm eff} \leq$ 2500 K (Lodders 1999) since the cross sections of FeH and CrH are approximately equal at 0.99 μm. A similar effect may occur in the J band since the 0–1 band of FeH at ∼1.19 μm is strong in the spectra of L dwarfs (Cushing et al. 2003; McLean et al.

TABLE 7
CH_4 Features in Dwarf Spectra

Vacuum Wavelength (μm)	
1.6149080	1.6382678
1.6173155	1.6575994
1.6193378	1.6622256
1.6215579	1.6940340
1.6237635	1.6976493
1.6261759	1.7006882
1.6283867	1.7042962
1.6308079	1.7075190
1.6332215	1.7117420
1.6356431	...

2003) and the cross sections of CrH and FeH are also approximately equal at these wavelengths (Dulick et al. 2003).

CH_4.—The appearance of overtone and combination bands of CH_4 in the near-infrared spectra of late-type dwarfs is the defining characteristic of the T spectral class (Burgasser et al. 2002b). For the most part, published spectra of T dwarfs have low spectral resolution so the absorption bands appear relatively smooth. At a resolving power of $R \approx 1200$, it should be possible to identify individual CH_4 absorption features. To this end, we have compared an FTS emission spectrum of CH_4 (Nassar & Bernath 2003) with our spectrum of 2MASS J0559−1404 (T5) to search for any common features. The CH_4 spectrum, which was obtained at a temperature of 1000 K, covers from 1.56 to 5.0 μm at a resolving power of $R \approx$ 160,000. We smoothed the CH_4 spectrum to $R = 1200$ and resampled it onto the wavelength grid of 2MASS J0559−1404.

Figure 4 shows the spectra of CH_4 and 2MASS J0559−1404 (T5) centered on the $2\nu_3$ band ($\sim$1.6 μm). Nineteen features common to the two spectra are shown by dotted lines and are listed in Table 7. Although the spectra of the T dwarfs exhibit a series of roughly equidistant absorption features from 1.615 to 1.65 μm, the same series of emission features in the CH_4 spectrum are truncated at $\sim$1.635 μm. In addition, the strong absorption feature in the T dwarf spectra at 1.665 μm is missing in the CH_4 emission spectrum. The lack of emission of features at these wavelengths is most likely caused by self-absorption due to room temperature CH_4 in the apparatus (Nassar & Bernath 2003). These features can also be seen throughout the T dwarf sequence (McLean et al. 2003).

The Q-branch of the ν_3 fundamental band of CH_4 at 3.33 μm has also been detected in the spectra of two late-type L dwarfs, 2MASS J1507−1627 (L5) and 2MASS J0825+2115 (L7.5), by Noll et al. (2000). Although the detection is secure, the spectra were of fairly low S/N. Figure 5 shows the emission spectrum of CH_4 in the bottom panel and the spectra of 2MASS J0825+2115 and SDSS J1254−0122 (T2) in the top panel. The dwarf spectra ($R \approx 300$) were obtained using the IRCS on Subaru (see § 2.2) and have a higher S/N than the Noll et al. (2000) spectra. The Q-branch is clearly seen in both dwarf spectra, while the broad P- and R-branches can be seen in the spectrum of SDSS J1254−0122.

3.1.2. *Atomic Features*

In order to identify the atomic features in the spectra of the M and L dwarfs, we used the high-resolution ($R = 100{,}000$) infrared spectral atlas of Arcturus (Hinkle et al. 1995) and a spectrum of Arcturus obtained with SpeX. Arcturus' spectral type is K1.5 III, cool enough that most of the atomic features present in its spectrum will also be present in the spectra of early-type M dwarfs. We first identified absorption features present in both the SpeX Arcturus spectrum and the spectrum of Gl 229A (M1 V) and then searched the Arcturus atlas for the feature identifications. The absorption features, which include neutral lines of Ti, Al, Si, Ca, Fe, Mg, K, and Na, are listed in Table 6 and shown in Figures 6–15.

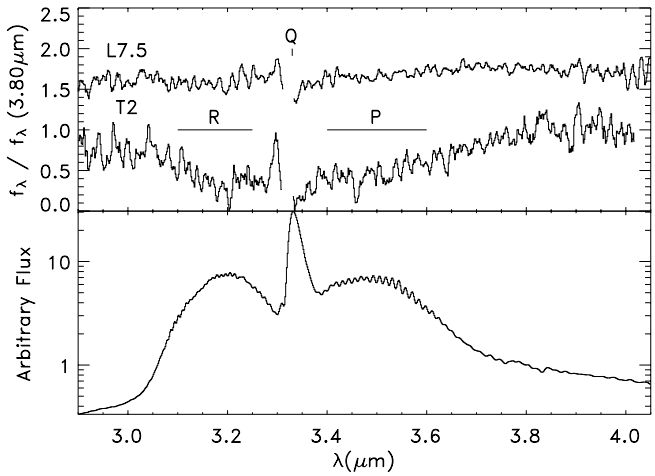

FIG. 5.—*Bottom*: CH_4 emission spectrum. *Top*: Spectra of 2MASS J0825+2115 (L7.5) and SDSS J1254−0122 (T2). Note that the CH_4 spectrum is plotted on a logarithmic scale. The positions of the P-, Q-, and R-branches are indicated.

McLean et al. (2000) reported a detection of the Rb I line at 1.3234 μm in the spectra of L dwarfs and the Cs I line at 1.359 μm in the spectrum of 2MASS J1507−1627 (L5). We see no evidence of these lines nor of any other lines of Rb and Cs (Fisher et al. 1959) in our spectra. There is an absorption feature at 1.3234 μm coincident with the position of an Rb line, but this feature can be seen in the spectrum of vB 10 (M8 V) and therefore is most likely due to H_2O.

3.2. *Spectral Morphology*

Having identified both atomic and molecular absorption features in the spectra of the M, L, and T dwarfs, we now give a detailed description of the spectral morphology of the spectra in the z, J, H, K, and L bands. Figures 6–15 show a sequence of the M, L and T dwarfs in each of the z, J, H, K, and L bands along with the identified features.

3.2.1. *z Band*

The z-band spectra of the early M dwarfs contain mainly atomic absorption features of Ti, Fe, Ca, Si, and Mg. Most prominent is a series of 12 Ti features centered at 0.97 μm arising from the $a\,^5F$–$z\,^5F^o$ multiplet. These features are clearly discernible down to a spectral type of M9 and disappear at $\sim$L1. The band head of the Wing-Ford band of FeH (0–0 band of the $F\,^4\Delta$–$X\,^4\Delta$ system) at 0.9969 μm, along with the FeH Q-branch feature at 1.006 μm, already appears quite strong at a spectral type of M1. At later spectral types, the Wing-Ford band replaces the atomic features as the dominant carrier of absorption features in this wavelength range. We have identified 32 FeH features in this wavelength range (Cushing et al. 2003). These features, along with the 0–0 band head and Q-branch feature, weaken considerably by a spectral type of $\sim$L7. The band head is also present in the spectrum of the T5 dwarf 2MASS J0559−1404 (see Burgasser et al. 2002a). The 0–0 band of the $A\,^4\Pi$–$X\,^4\Sigma^-$ system of VO at $\sim$1.06 μm appears at a spectral type of $\sim$M5, peaks in strength at

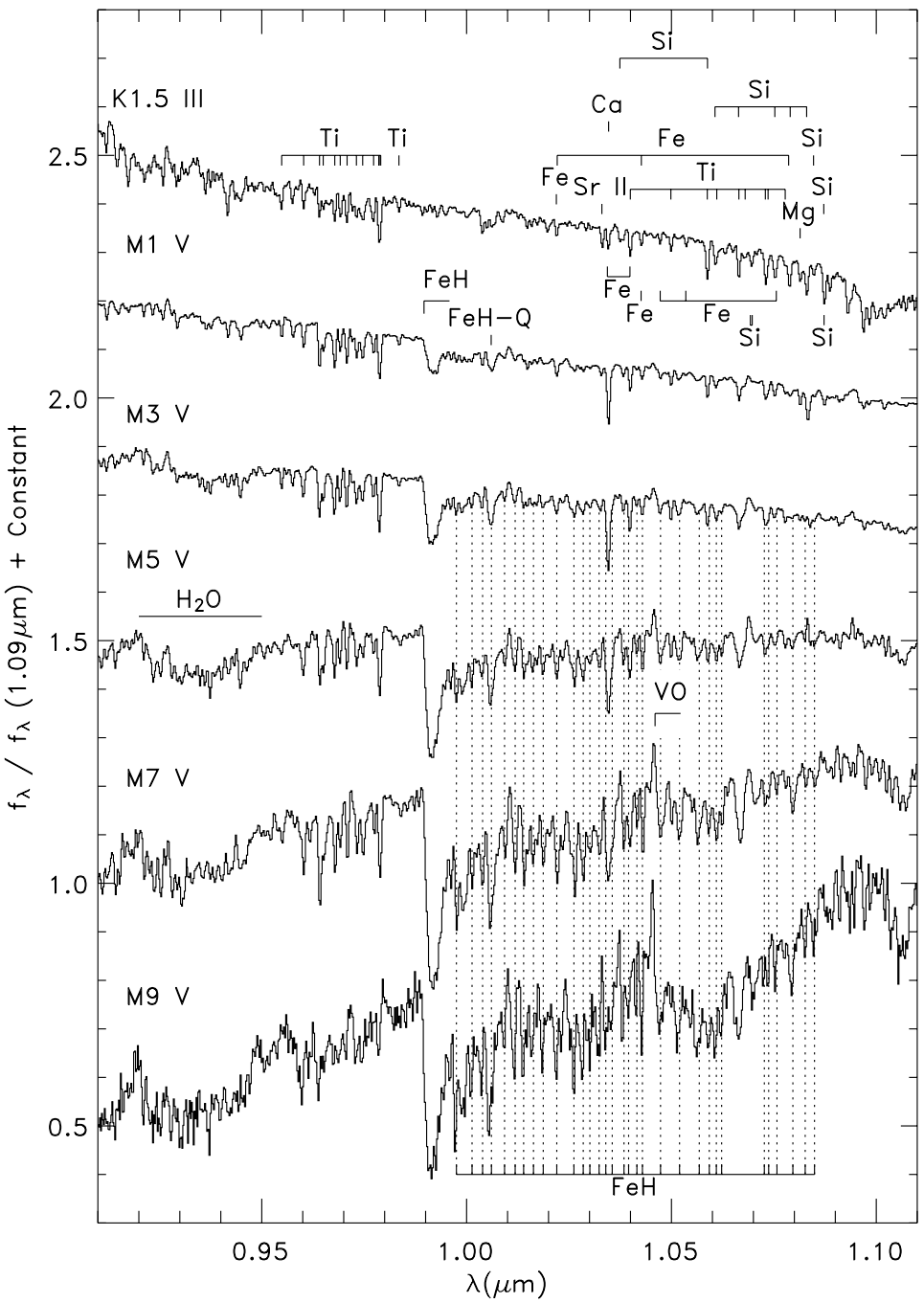

FIG. 6.—The *z*-band spectra of Arcturus (K1.5 III), Gl 229A (M1 V), Gl 388 (M3 V), Gl 51 (M5 V), νB 8 (M7 V), and LHS 2924 (M9 V). The most prominent molecular and atomic features are indicated.

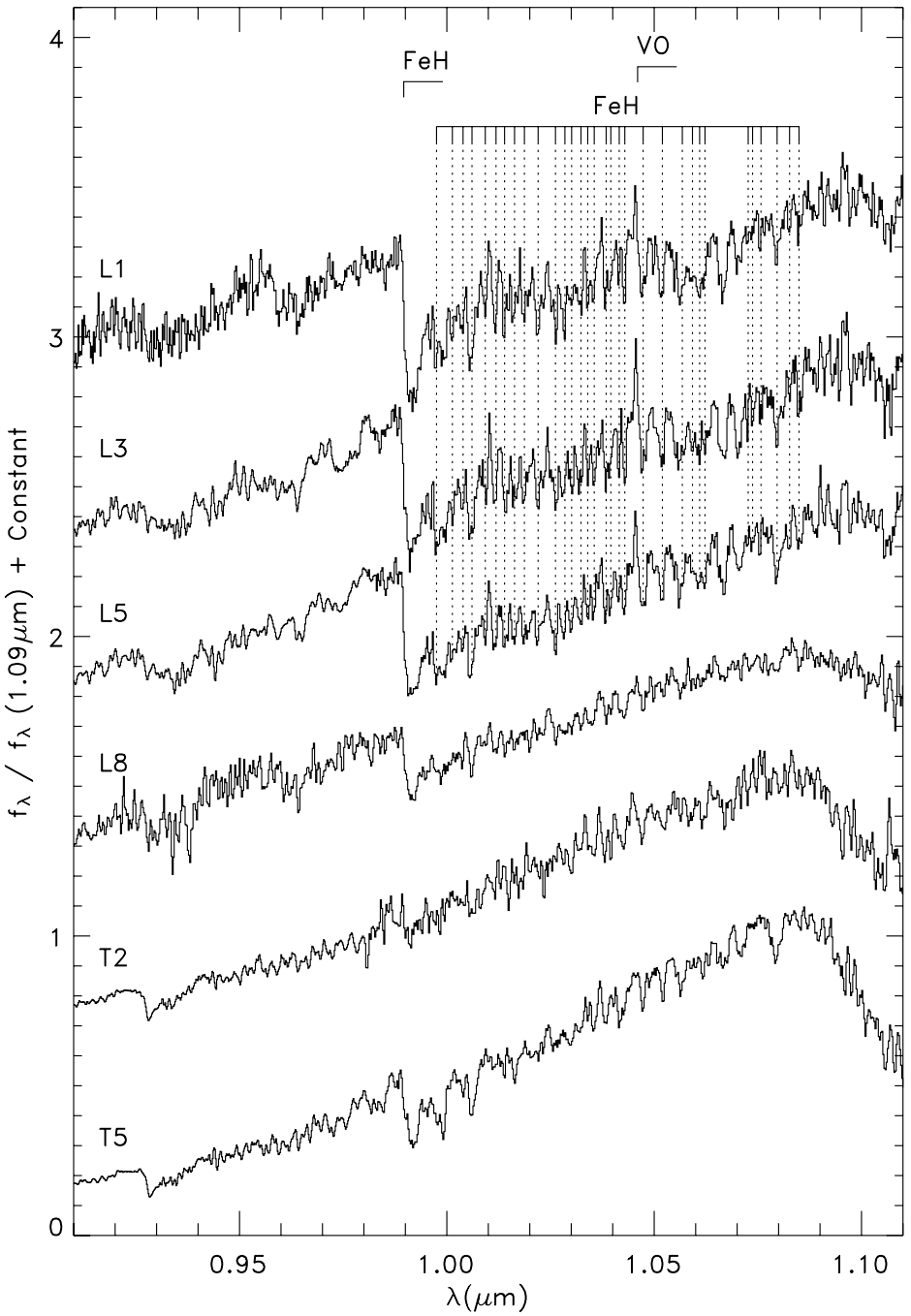

FIG. 7.—The *z*-band spectra of 2MASS J1439+1929 (L1), 2MASS J1506+1321 (L3), 2MASS J1507−1627 (L5), DENIS J0255−4700 (L8), SDSS J1254−0122 (T2), and 2MASS J0559−1404 (T5). The most prominent molecular and atomic features are indicated.

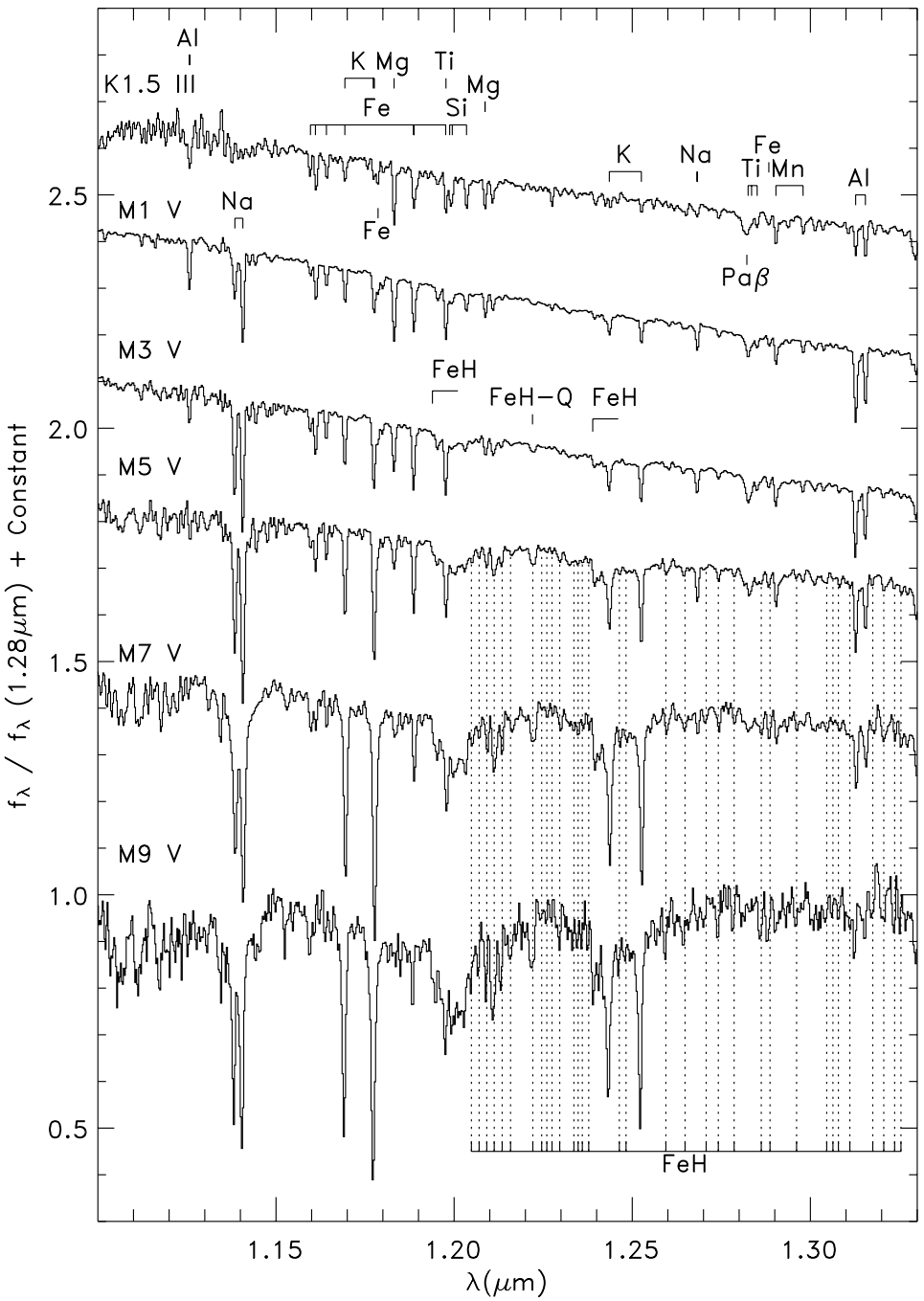

FIG. 8.—*J*-band spectra of Arcturus (K1.5 III), Gl 229A (M1 V), Gl 388 (M3 V), Gl 51 (M5 V), vB 8 (M7 V), and LHS 2924 (M9 V). The most prominent molecular and atomic features are indicated.

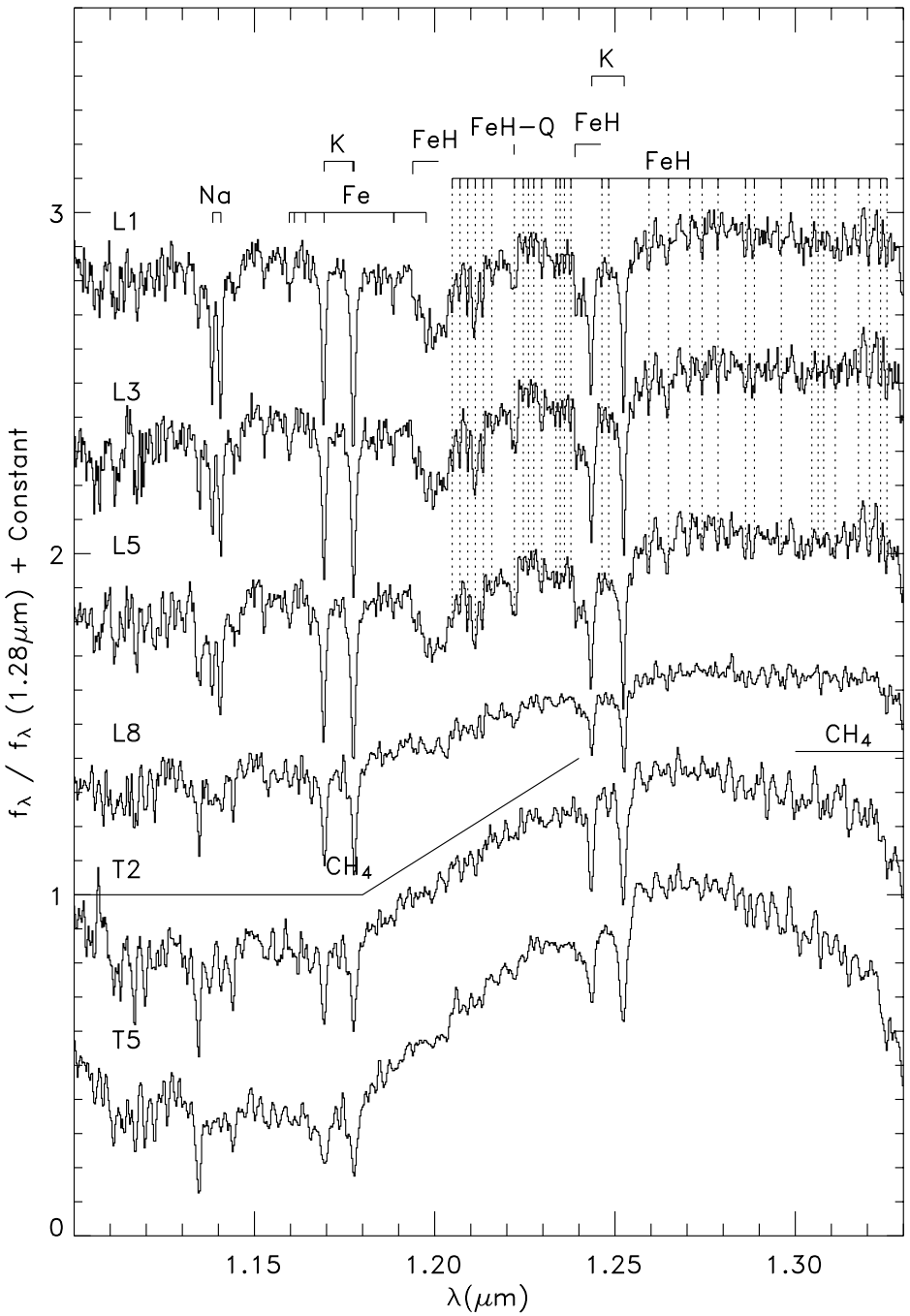

FIG. 9.—*J*-band spectra of 2MASS J1439+1929 (L1), 2MASS J1506+1321 (L3), 2MASS J1507−1627 (L5), DENIS J0255−4700 (L8), SDSS J1254− 0122 (T2), and 2MASS J0559−1404 (T5). The most prominent molecular and atomic features are indicated.

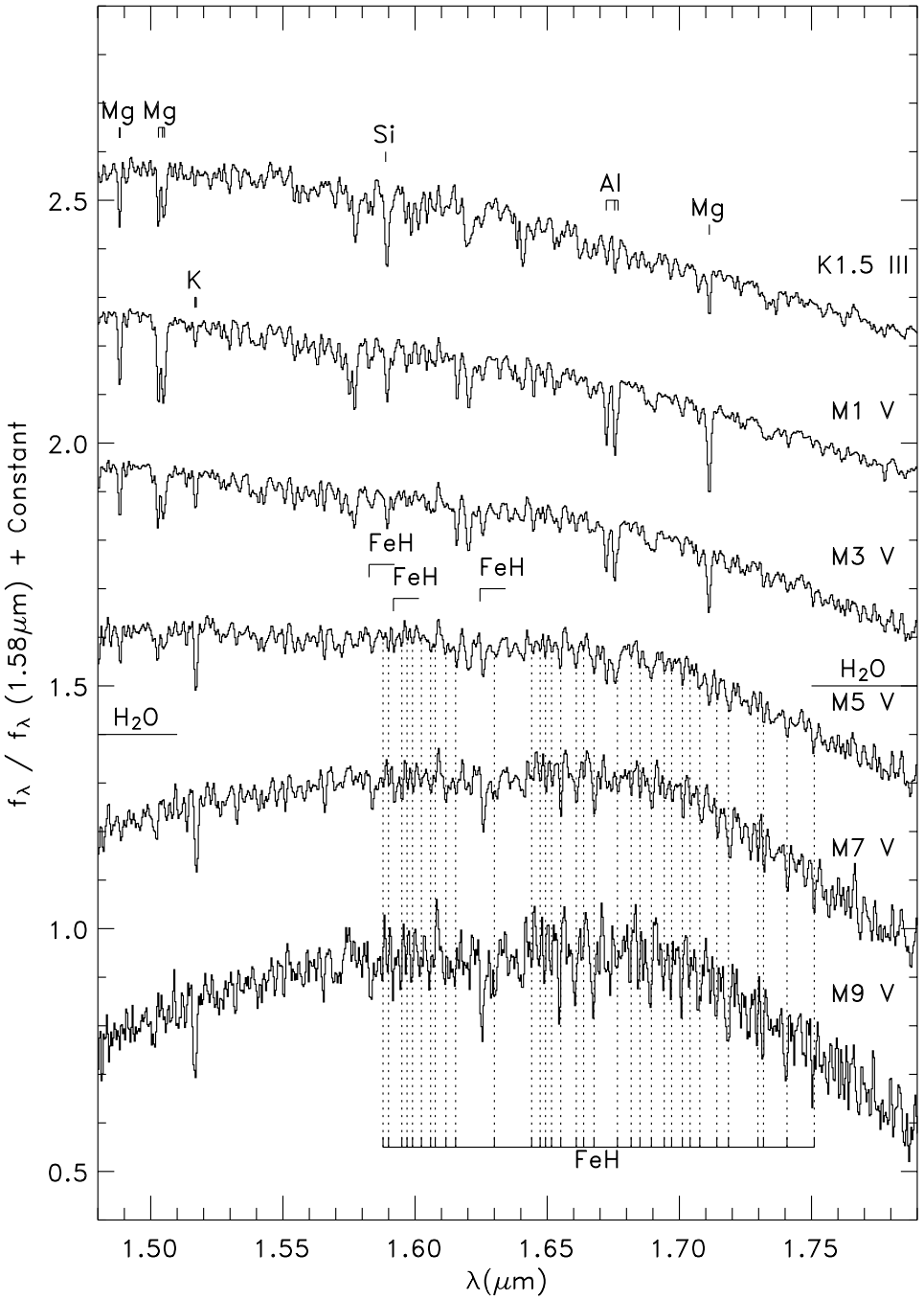

FIG. 10.—*H*-band spectra of Arcturus (K1.5 III), Gl 229A (M1 V), Gl 388 (M3 V), Gl 51 (M5 V), vB 8 (M7 V), and LHS 2924 (M9 V). The most prominent molecular and atomic features are indicated.

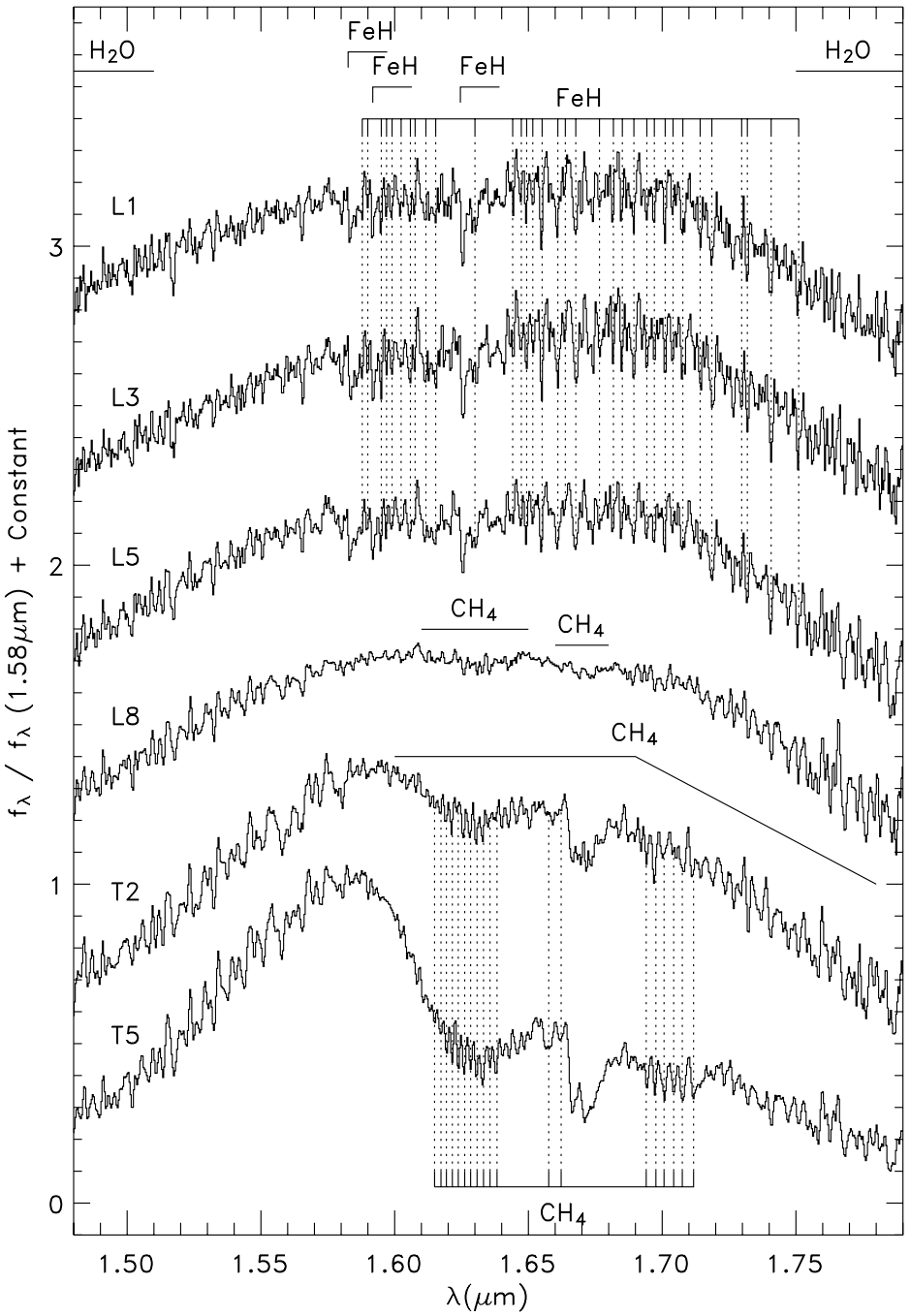

FIG. 11.—*H*-band spectra of 2MASS J1439+1929 (L1), 2MASS J1506+1321 (L3), 2MASS J1507−1627 (L5), DENIS J0255−4700 (L8), SDSS J1254−0122 (T2), and 2MASS J0559−1404 (T5). The most prominent molecular and atomic features are indicated.

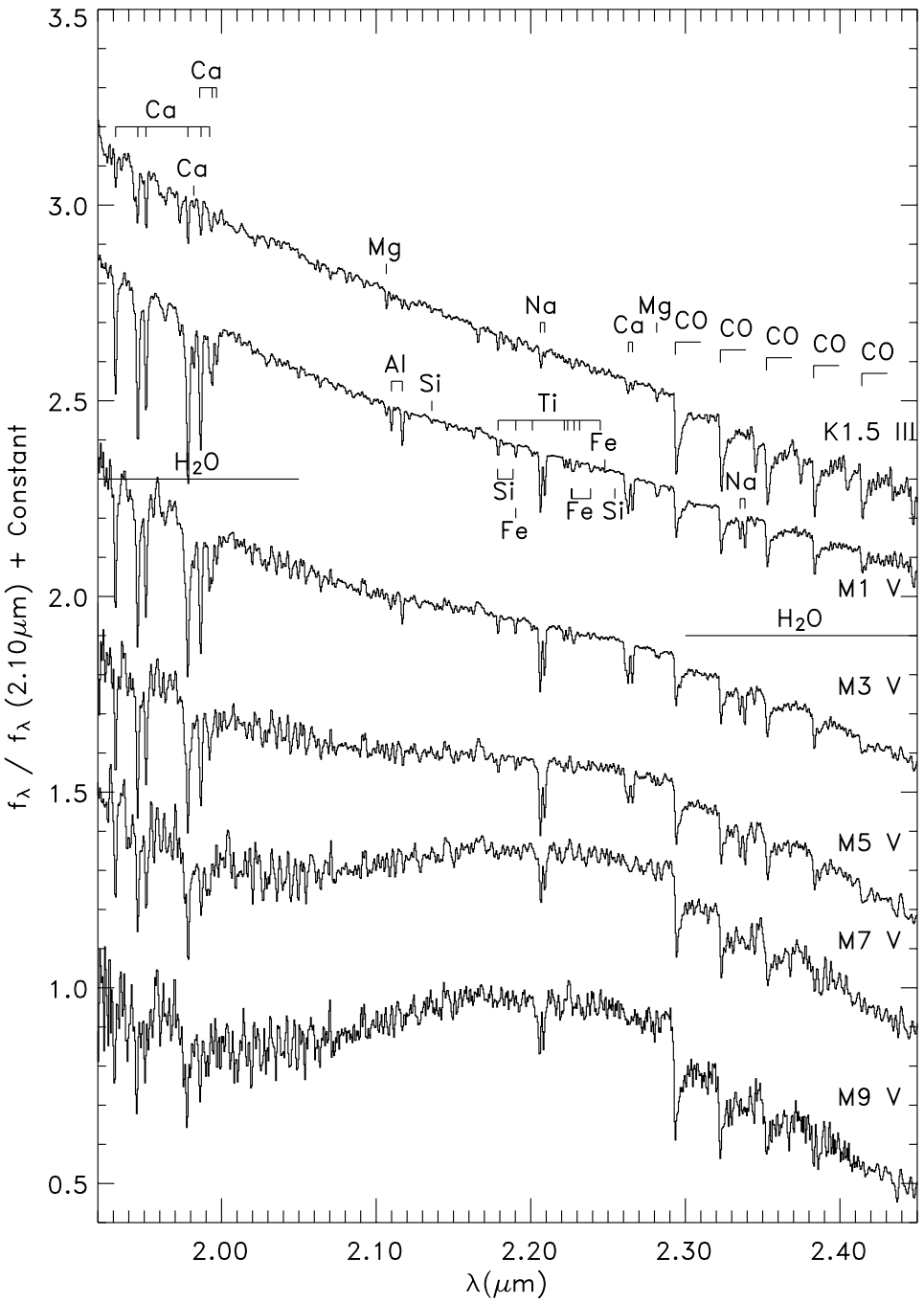

FIG. 12.—*K*-band spectra of Arcturus (K1.5 III), Gl 229A (M1 V), Gl 388 (M3 V), Gl 51 (M5 V), vB 8 (M7 V), and LHS 2924 (M9 V). The most prominent molecular and atomic features are indicated.

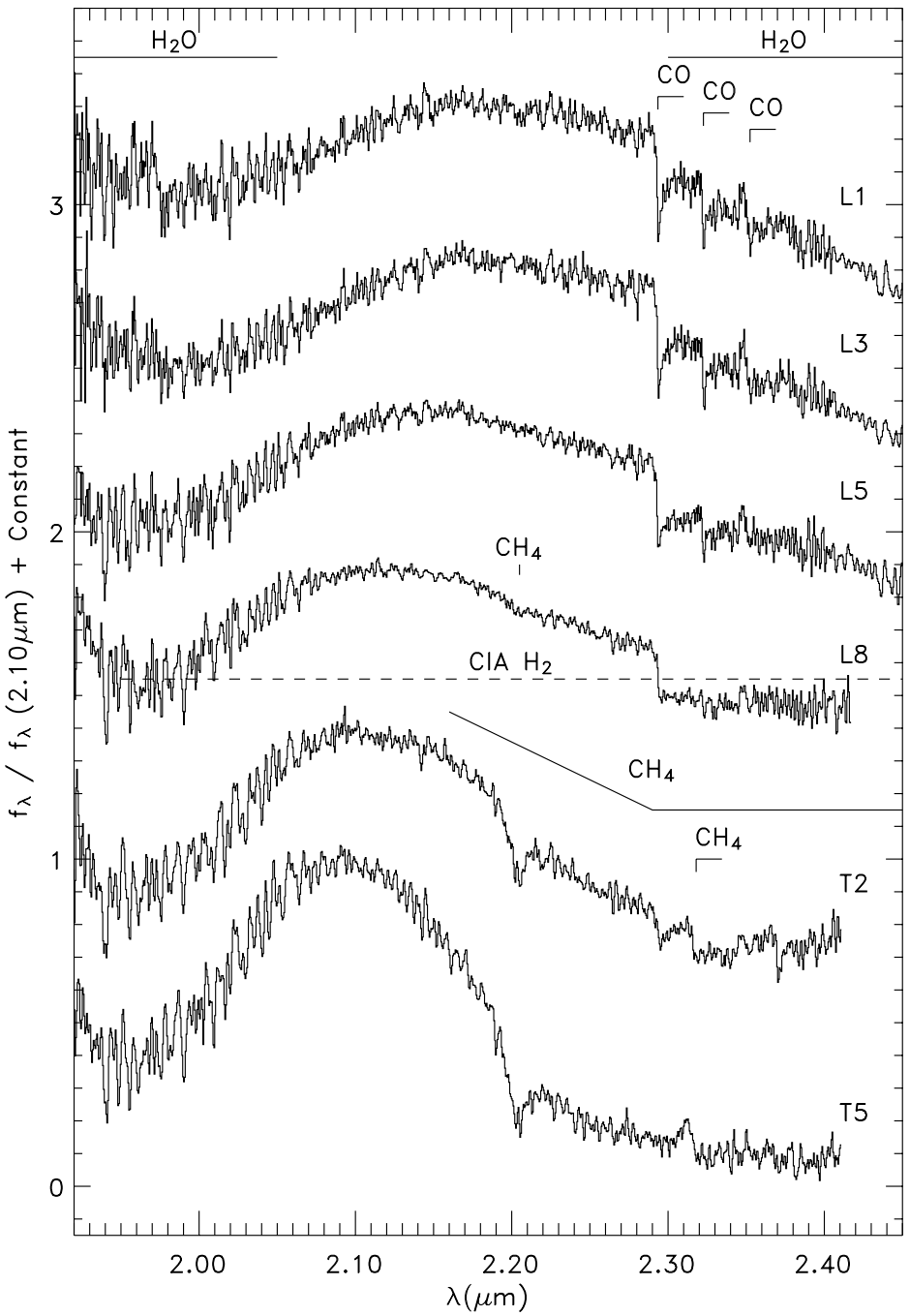

FIG. 13.—*K*-band spectra of 2MASS J1439+1929 (L1), 2MASS J1506+1321 (L3), 2MASS J1507−1627 (L5), DENIS J0255−4700 (L8), SDSS J1254−0122 (T2), and 2MASS J0559−1404 (T5). The most prominent molecular and atomic features are indicated.

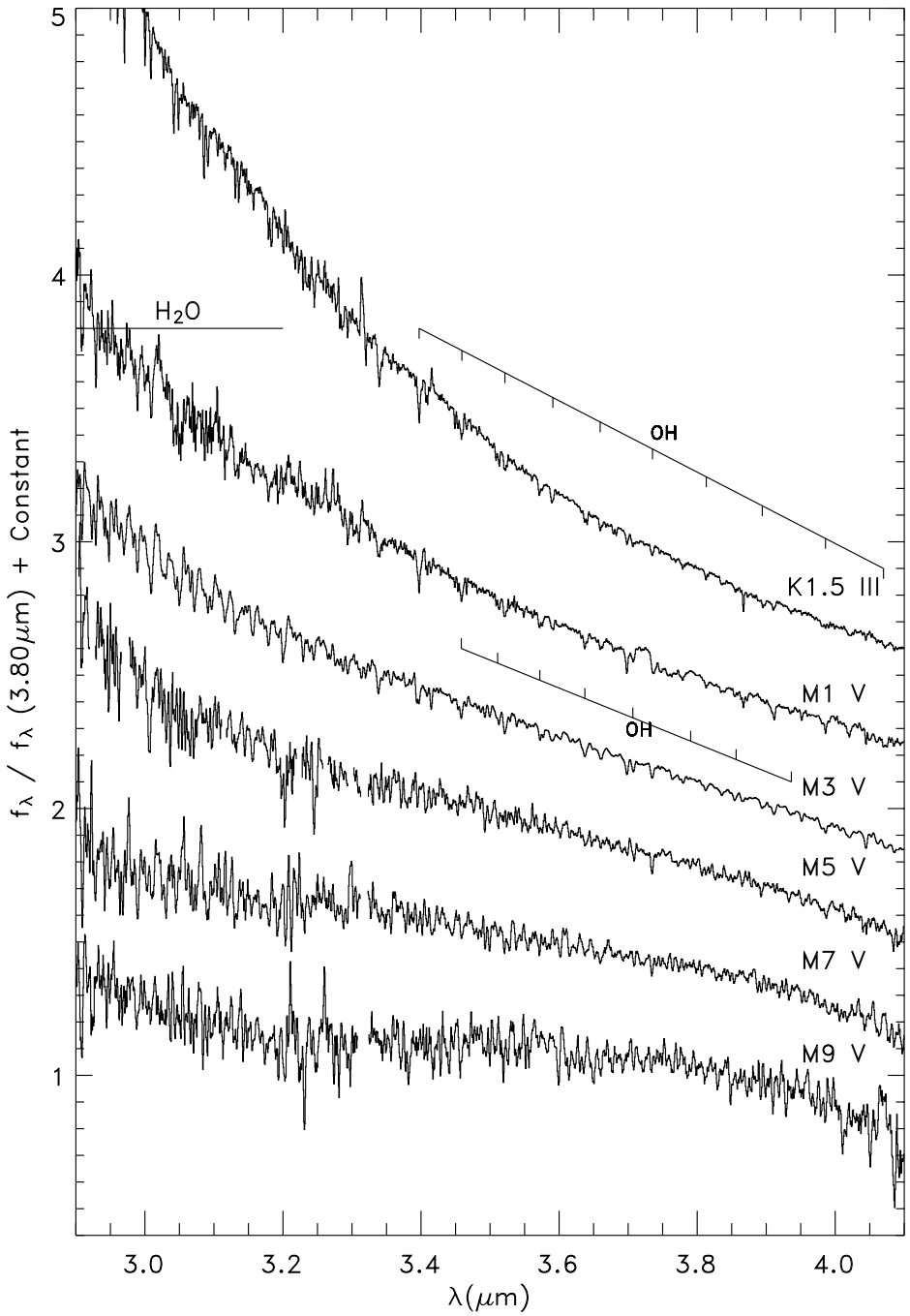

FIG. 14.—*L*-band spectra of Arcturus (K1.5 III), Gl 229A (M1 V), Gl 388 (M3 V), Gl 51 (M5 V), vB 8 (M7 V), and LHS 2924 (M9 V). The most prominent molecular and atomic features are indicated.

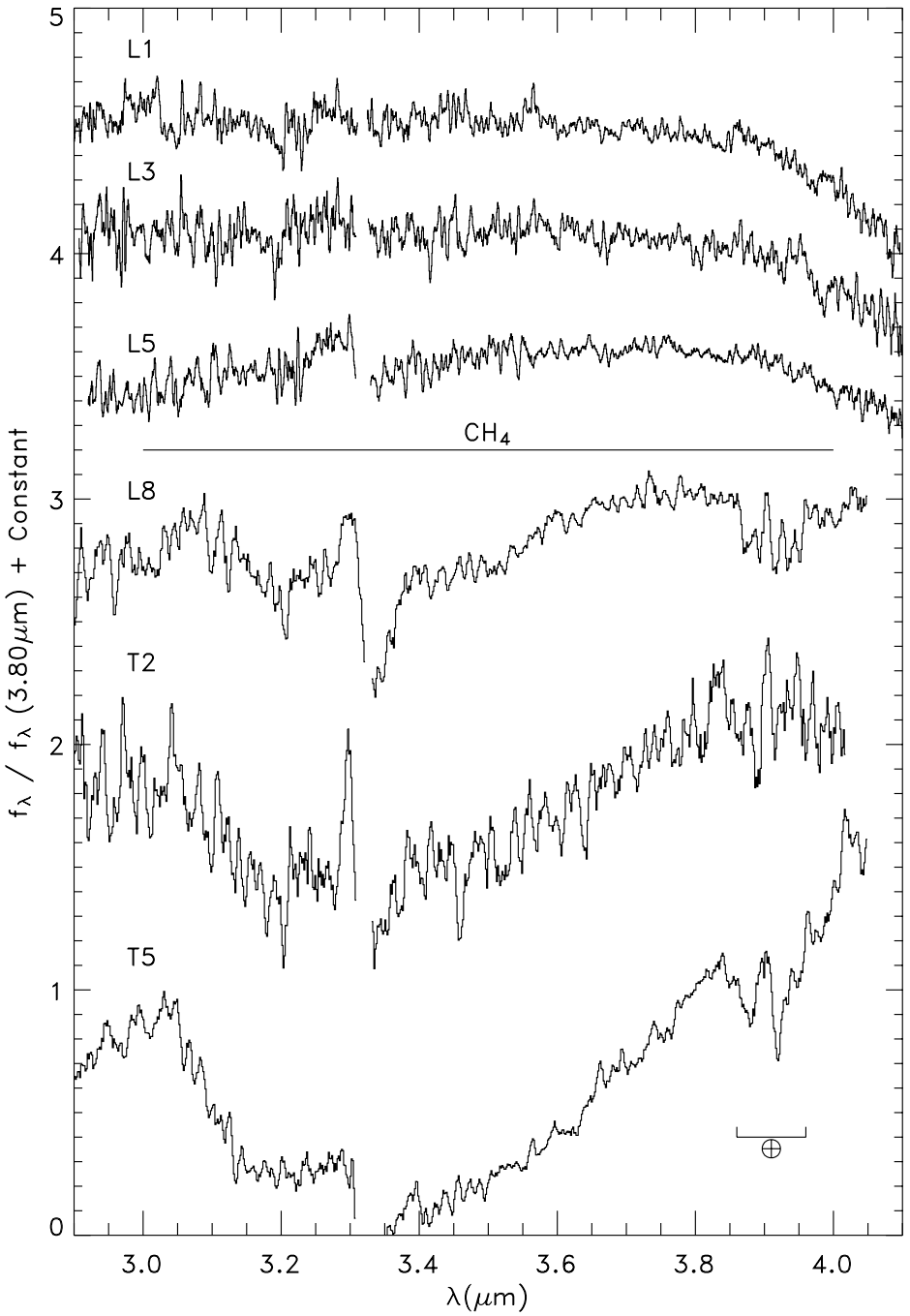

FIG. 15.—*L*-band spectra of 2MASS J1439+1929 (L1), 2MASS J1506+1321 (L3), 2MASS J1507−1627 (L5), DENIS J0255−4700 (L8), SDSS J1254−0122 (T2), and 2MASS J0559−1404 (T5). The most prominent molecular and atomic features are indicated. The absorption features seen in the spectra of DENIS J0255−4700 and 2MASS J0559−1404 centered at ∼3.9 μm are due to incomplete removal of the N_2O telluric feature.

M9, and then disappears by L5 (see § 3.1.1). Finally, the overall spectral shape becomes progressively redder with spectral type.

3.2.2. *J Band*

The *J* band contains the most prominent atomic features in the spectra of M and L dwarfs: the Na doublet at 1.14 μm and the two K doublets at 1.175 and 1.25 μm. Early M dwarf spectra also exhibit absorption features due to Fe, Mg, Ti, Si, H, and Mn, but most of these features weaken in the mid- to late-type M dwarfs. However, the Fe feature at 1.189189 μm persists to a spectral type of ~L5. The 0–1 band head of FeH ($F\,^4\Delta$–$X\,^4\Delta$ system) at 1.1939 μm and the associated *Q*-branch feature at 1.22210 μm, along with the 1–2 band head at 1.2389 μm, first appear at a spectral type of M3 and strengthen through the M sequence. Beginning at a spectral type of ~M5, 33 additional FeH absorption features can also be seen in the range 1.2–1.3 μm (Cushing et al. 2003). At a spectral type of ~L1, the only remaining atomic features are the Na and K lines and possibly a few weak Fe features at ~1.155 μm. The Na feature at 1.14 μm and the FeH features are not apparent at a spectral type of ~L7, but the K lines persist through the T sequence (McLean et al. 2003). As with the *z* band, the overall spectral shape of the *J* band becomes progressively redder with spectral type. Finally, CH_4 bands in the range 1.15–1.25 μm and CH_4 and H_2O bands longward of 1.28 μm cause the *J*-band spectra of the T dwarfs to become peaked at ~1.27 μm.

3.2.3. *H Band*

The *H* band is the most difficult wavelength range in which to identify features in the spectra of early M dwarfs because it contains many relatively weak absorption features. Only a few doublets and triplets of Mg, Si, Al, and K are clearly evident. Meyer et al. (1998) identify eight second-overtone ($\Delta\nu = 3$) band heads of ^{12}CO in $R = 3000$ spectra of K and M dwarfs. However, we cannot unambiguously identify any of these bands. H_2O bands on either side of the *H* band also begin to appear at a spectral type of ~M4 and strengthen through the M, L, and T sequence.

A new band of FeH, tentatively identified as the $E\,^4\Pi$–$A\,^4\Pi$ system by Wallace & Hinkle (2001), appears at ~M5 and becomes the dominant carrier of absorption features from 1.59 to 1.75 μm (Cushing et al. 2003). At the same time, the atomic absorption features of Mg, Si, and Al weaken and disappear, except for the K I line at 1.516 μm, which persists to ~L5. Finally, the appearance of the $2\nu_3$ and $2\nu_2 + \nu_3$ bands of CH_4 at ~1.67 μm signals the transitions to the T spectral class although weak CH_4 absorption features are also found in the spectra of the late L dwarfs (McLean et al. 2003; see also § 4.2). Both bands strengthen through the T sequence (McLean et al. 2003).

3.2.4. *K Band*

The *K*-band spectra of early M dwarfs also exhibit atomic features of Ca, Mg, Al, Si, Na, Ti, and Fe. The most prominent features are the series of Ca lines at 1.95 μm, the Na doublets at 2.21 and 2.34 μm, and the Ca doublet at 2.26 μm. These features all weaken with increasing spectral type; the 2.26 μm Ca doublet disappears at ~M7, while the 1.95 μm Ca lines, as well as the Na lines, disappear at ~L0. Also prominent are the series of first-overtone band heads ($\Delta\nu = +2$) of ^{12}CO extending redward from 2.29 μm. Beginning with the 6–4 band head at 2.41414 μm and moving to lower transitions, the band heads disappear through the M and L dwarfs until only the 2–0 is present at a spectral type of T2. H_2O absorption bands also appear on either side of the *K* band at a spectral type of ~M4 and strengthen through the M, L, and T sequence. CH_4 absorption at 2.2 μm first appears in the late-type L dwarfs (see also § 4.2) and continues to strengthen through the T sequence suppressing the *K*-band flux. The *K*-band flux in T dwarfs is further suppressed by collision-induced H_2 absorption (Borysow 2002). Although this opacity source exhibits no band heads or distinct spectral features, its presence can be inferred from model atmospheres (M. Marley 2004, private communication).

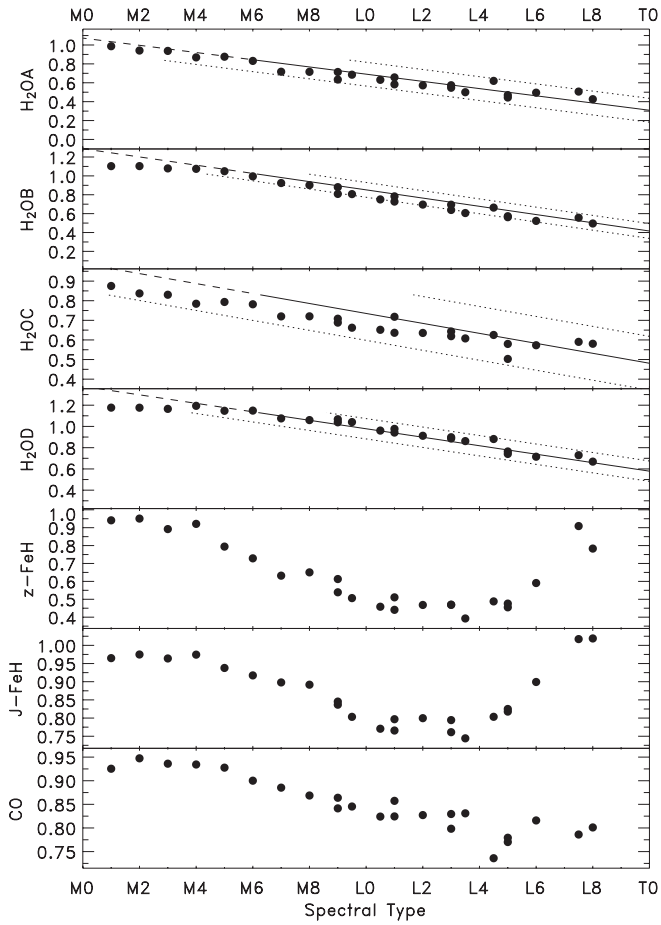

FIG. 16.—Values of the spectral indices of McLean et al. (2003) for the M and L dwarfs in our sample as a function of spectral type. Also shown for the H_2O indices are the best-fitting linear relations derived by McLean et al. (2003) from their data. The solid lines show the spectral type range over which the lines were derived (M6–T8), while the dashed lines show the extension of the solid lines to earlier spectral types. The dotted lines denote the 3 σ uncertainties on the relations.

3.2.5. *L Band*

The *L*-band spectra of M and L dwarfs are dominated by molecular absorption features due mainly to H_2O. However, there are also absorption features due to the $\Delta\nu = +1$ bands of OH. Features from both the 1–0 and 2–1 bands are seen (Wallace & Hinkle 2002). Like the *z* and *J* bands, the overall slope of the spectra becomes progressively redder with spectral type until the spectra are nearly flat at a spectral type of L1. At a spectral type of ~L5, the ν_3 fundamental band of CH_4 appears in the spectra (Noll et al. 2000). At first, only the *Q*-branch is present in the spectra, but the *P*- and *R*-branches are apparent at T2, and the band becomes saturated by a spectral type of T5.

3.3. *Spectral Indices*

As described in the previous section, the overall infrared spectral morphology of the M, L, and T dwarfs, as well as the

TABLE 8
K I Equivalent Widths

Object (1)	Spectral Type (2)	EW (Å) 1.169 μm (3)	1.177 μm (4)	1.244 μm (5)	1.253 μm (6)
Gl 229A	M1 V	0.5 ± 0.1	0.8 ± 0.1	0.5 ± 0.1	0.5 ± 0.1
Gl 411	M2 V	0.5 ± 0.1	0.6 ± 0.1	0.3 ± 0.1	0.4 ± 0.1
Gl 388	M3 V	0.9 ± 0.1	1.4 ± 0.1	0.7 ± 0.1	0.8 ± 0.1
Gl 213	M4 V	0.7 ± 0.1	1.5 ± 0.1	0.8 ± 0.1	0.7 ± 0.1
Gl 51	M5 V	1.7 ± 0.1	2.9 ± 0.1	1.3 ± 0.1	1.7 ± 0.1
Gl 406	M6 V	3.0 ± 0.1	4.7 ± 0.1	2.4 ± 0.1	2.9 ± 0.1
vB 8	M7 V	4.2 ± 0.1	6.4 ± 0.2	3.2 ± 0.2	4.3 ± 0.1
vB 10	M8 V	5.0 ± 0.2	7.0 ± 0.2	3.5 ± 0.2	4.7 ± 0.2
LP 944−20	M9 V	5.5 ± 0.3	7.9 ± 0.2	3.8 ± 0.3	5.2 ± 0.3
LHS 2924	M9 V	5.6 ± 0.3	8.8 ± 0.3	4.1 ± 0.3	5.3 ± 0.3
BRI 0021−0214	M9.5 V	6.3 ± 0.3	9.1 ± 0.4	4.6 ± 0.4	6.4 ± 0.4
2MASS J0746+2000AB	L0.5	6.7 ± 0.3	10.2 ± 0.4	4.8 ± 0.4	6.6 ± 0.4
2MASS J1439+1929	L1	6.9 ± 0.4	10.5 ± 0.4	4.9 ± 0.4	7.3 ± 0.5
2MASS J0208+2542	L1	6.4 ± 0.5	10.4 ± 0.7	3.8 ± 0.6	6.3 ± 0.5
Kelu-1	L2	6.3 ± 0.4	9.1 ± 0.5	3.8 ± 0.5	6.4 ± 0.5
2MASS J1146+2230AB	L3	6.9 ± 0.3	10.1 ± 0.3	5.2 ± 0.3	7.4 ± 0.3
2MASS J1506+1321	L3	8.4 ± 0.5	11.1 ± 0.5	5.3 ± 0.5	7.7 ± 0.5
2MASS J0036+1821	L3.5	9.0 ± 0.5	12.3 ± 0.5	5.2 ± 0.5	8.2 ± 0.5
2MASS J2224−0158	L4.5	6.7 ± 0.8	12.0 ± 0.6	4.7 ± 0.4	6.5 ± 0.5
2MASS J1507−1627	L5	8.6 ± 0.5	11.8 ± 0.4	4.1 ± 0.4	7.8 ± 0.5
SDSS J0539−0059	L5	8.8 ± 0.4	12.1 ± 0.4	4.0 ± 0.4	8.3 ± 0.5
2MASS J1515+4847	L6	6.9 ± 0.7	10.5 ± 0.5	3.4 ± 0.4	6.2 ± 0.4
2MASS J0825+2115	L7.5	4.4 ± 0.3	5.1 ± 0.2	2.8 ± 0.1	3.9 ± 0.2
DENIS J0255−4700	L8	5.8 ± 0.6	7.0 ± 0.3	2.1 ± 0.2	3.9 ± 0.2
SDSS J1254−0122	T2	5.6 ± 0.7	9.3 ± 0.4	3.9 ± 0.3	6.8 ± 0.4
2MASS J0559−1404	T5	8.7 ± 1.0	13.2 ± 0.9	3.7 ± 0.3	8.4 ± 0.5

strengths of many of the absorption features including H_2O, FeH, and CO, exhibits a smooth variation with spectral type. To quantify these variations, numerous spectral indices, ratios of fluxes in particular wavelength intervals chosen to measure the changes in spectral morphology, or depths of specific absorption features have been defined (e.g., Tokunaga & Kobayashi 1999; Burgasser et al. 2002b; Geballe et al. 2002; Testi et al. 2001; Reid et al. 2001; McLean et al. 2003). In particular, McLean et al. (2003) have defined a suite of indices for late-type dwarfs (M6–T8) using spectra with resolving powers similar to that of our spectra ($R = 2000$). The H_2OA, H_2OB, H_2OC, and H_2OD indices measure the strength of the 1.35, 1.4, 1.7, and 2.0 μm H_2O water bands, respectively, while the *z*-FeH, *J*-FeH, and CO indices measure the strengths of the 0–0 band of FeH at 0.99 μm, the 0–1 FeH band head at 1.17 μm, and the ^{12}CO 2–0 band head at 2.29 μm, respectively. We have computed these indices for the dwarfs in our sample in order to determine how well they characterize the spectra of dwarfs with spectral types earlier than M6 V. Figure 16 shows the values of the indices as a function of spectral type for the M and L dwarfs in our sample; a smaller value implies stronger absorption.

The H_2OA and H_2OC indices show a good correlation with spectral type throughout the entire M and L sequence. However, the continuum flux window for the H_2OA index (1.313 μm) is centered on the Al I doublet at 1.3130514 μm (see § 3.4) and, as a result, cannot be used for M dwarfs with spectral types earlier than ~M8. The H_2OB and H_2OD indices are roughly constant from M0 to M4, at which point they decrease steadily through the M, L, and T sequence as shown by McLean et al. (2003). Also shown in Figure 16 are the best-fitting straight lines (*solid*/*dashed*) and ±3 σ errors (*dotted*) derived by McLean et al. (2003). All of our data are within the 3 σ errors, but our H_2OC indices lie systematically below the line defined by McLean et al. (2003). It is unclear what causes the systematic differences for the H_2OC index.

The two FeH indices show similar behavior. The indices are roughly constant from M0 to ~M4, at which point they decrease steadily until a spectral type of ~L0. The indices are roughly constant from L0 to L5, although there is significant scatter. The FeH bands disappear by the end of the L sequence (the indices approach unity), but the 0–0 band reappears in the mid-type T dwarfs (Burgasser et al. 2002a; McLean et al. 2003). Finally, the CO index values, like the H_2OB, H_2OD, *J*-FeH, and *z*-FeH indices, are roughly constant from M0 to ~M4 and then decrease through the entire L sequence. The CO index, like the FeH indices, shows significant scatter in the L sequence. Overall, the McLean et al. (2003) indices can be used to constrain spectral types only for those dwarfs later than M4.

3.4. *Equivalent Widths of Atomic Features*

We computed the equivalent widths (EWs) of the strongest atomic features in the spectra of the dwarfs. The EW and the variance of the EW, $\sigma^2_{\rm EW}$, are given by

$$\mathrm{EW} = \sum_{i=1}^{n} \left[1 - \frac{f(\lambda_i)}{f_c(\lambda_i)}\right] \Delta\lambda_i, \tag{4}$$

$$\sigma^2_{\rm EW} = \sum_{i=1}^{n} \Delta\lambda_i^2 \left[\frac{\sigma^2(\lambda_i)}{f_c^2(\lambda_i)} + \frac{f^2(\lambda_i)}{f_c^4(\lambda_i)} \sigma_c^2(\lambda_i)\right], \tag{5}$$

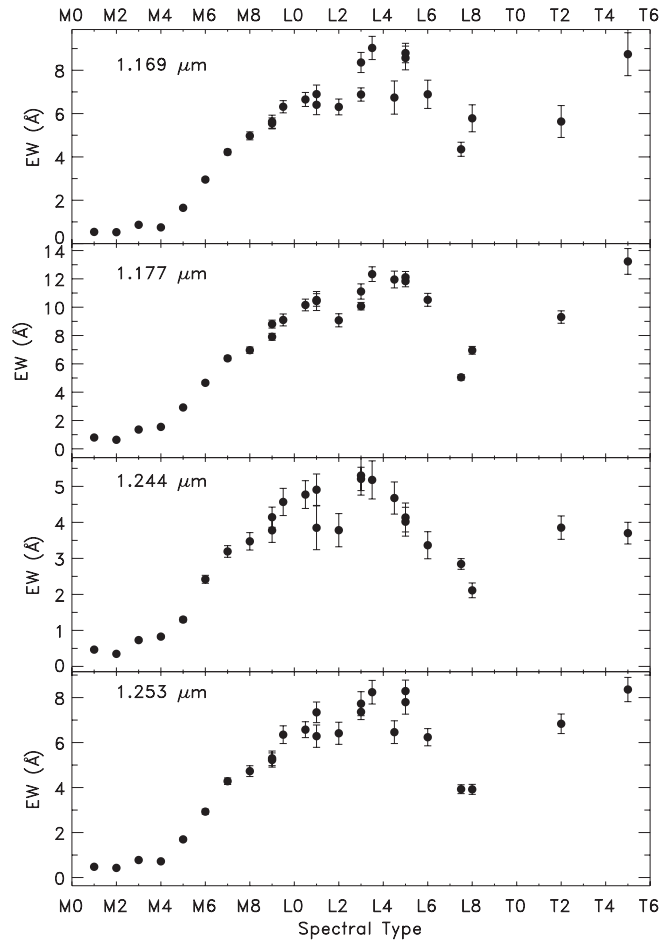

FIG. 17.—EWs of the K I lines in the spectra of the dwarfs in our sample as a function of spectral type.

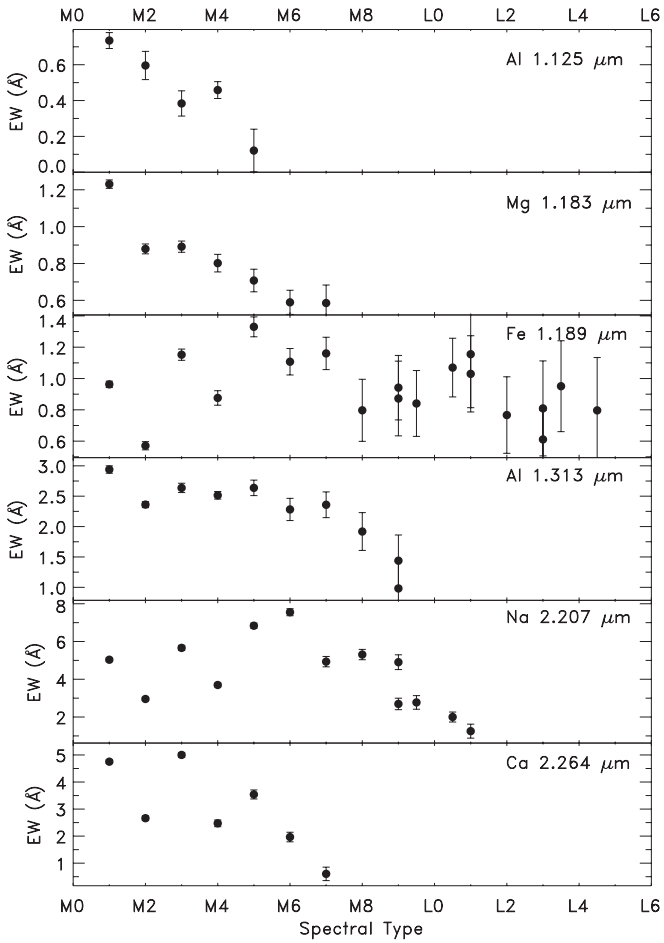

FIG. 18.—EWs of prominent lines of Al, Fe, Mg, Ca, and Na in the spectra of the dwarfs in our sample as a function of spectral type.

TABLE 9
EQUIVALENT WIDTHS OF OTHER LINES

		EW (Å)					
OBJECT (1)	SPECTRAL TYPE (2)	Al I 1.125 μm (3)	Mg I 1.183 μm (4)	Fe I 1.189 μm (5)	Al I 1.132 μm (6)	Na I 2.207 μm (7)	Ca I 2.264 μm (8)
Gl 229A	M1 V	0.7 ± 0.1	1.2 ± 0.1	1.0 ± 0.1	2.9 ± 0.1	5.0 ± 0.1	4.7 ± 0.1
Gl 411	M2 V	0.6 ± 0.1	0.9 ± 0.1	0.6 ± 0.1	2.4 ± 0.1	3.0 ± 0.1	2.7 ± 0.1
Gl 388	M3 V	0.4 ± 0.1	0.9 ± 0.1	1.2 ± 0.1	2.6 ± 0.1	5.7 ± 0.1	5.0 ± 0.1
Gl 213	M4 V	0.5 ± 0.1	0.8 ± 0.1	0.9 ± 0.1	2.5 ± 0.1	3.7 ± 0.1	2.5 ± 0.1
Gl 51	M5 V	0.1 ± 0.1	0.7 ± 0.1	1.3 ± 0.1	2.6 ± 0.1	6.8 ± 0.1	3.5 ± 0.2
Gl 406	M6 V	...	0.6 ± 0.1	1.1 ± 0.1	2.3 ± 0.2	7.6 ± 0.2	2.0 ± 0.2
vB 8	M7 V	...	0.6 ± 0.1	1.2 ± 0.1	2.4 ± 0.2	4.9 ± 0.3	0.6 ± 0.2
vB 10	M8 V	...	...	0.8 ± 0.2	2.0 ± 0.3	5.3 ± 0.3	...
LP 944−20	M9 V	...	...	0.9 ± 0.2	1.0 ± 0.4	2.7 ± 0.3	...
LHS 2924	M9 V	...	...	0.9 ± 0.2	1.4 ± 0.4	4.9 ± 0.4	...
BRI 0021−0214	M9.5 V	...	...	0.8 ± 0.2	...	2.8 ± 0.4	...
2MASS J0746+2000AB	L0.5	...	...	1.1 ± 0.2	...	2.0 ± 0.3	...
2MASS J1439+1929	L1	...	...	1.0 ± 0.2	...	1.3 ± 0.4	...
2MASS J0208+2542	L1	...	...	1.2 ± 0.3	...	...	...
Kelu-1	L2	...	...	0.8 ± 0.2	...	...	...
2MASS J1146+2230AB	L3	...	...	0.6 ± 0.2	...	...	...
2MASS J1506+1321	L3	...	...	0.8 ± 0.3	...	...	...
2MASS J0036+1821	L3.5	...	...	1.0 ± 0.3	...	...	...
2MASS J2224−0158	L4.5	...	...	0.8 ± 0.3	...	...	...

where $f(\lambda_i)$ and $f_c(\lambda_i)$ are the observed and estimated continuum flux densities, $\sigma(\lambda_i)$ and $\sigma_c(\lambda_i)$ are the errors in the observed and estimated continuum flux densities, n is the number of wavelength intervals across the feature, and $\Delta\lambda_i$ is the width of wavelength interval i. We estimated $f_c(\lambda_i)$, $\sigma(\lambda_i)$, and $\sigma_c(\lambda_i)$ following the procedure of Sembach & Savage (1992). A linear unweighted polynomial is fitted to the values of the continuum in the regions on either side of the feature in question to determine $f_c(\lambda_i)$. Assuming the fit to be good, $\sigma(\lambda_i)$ is determined a posteriori by setting it equal to the standard deviation, s, of the flux density values around $f_c(\lambda_i)$ in the fitting regions. The errors in the continuum, $\sigma_c(\lambda_i)$, are then computed by multiplying the covariance matrix produced by the least-squares fit by s and then using the standard error propagation formula, including the coefficient covariances (see eq. [A13] of Sembach & Savage 1992).

The strongest atomic features in the spectra of late-type dwarfs are the two K I doublets located at $\sim$1.175 and $\sim$1.245 μm. Their EWs are tabulated in Table 8 and are shown as a function of spectral type in Figure 17. Although there is some scatter, the EWs of all four lines show a similar behavior with spectral type: they are roughly constant until a spectral type of $\sim$M4, at which point they increase markedly and reach a maximum at a spectral type of $\sim$L3. The EWs then decrease through the late L dwarfs but appear to increase again in the T dwarfs. The strengthening of the K I lines in the early T dwarfs was originally noted by Burgasser et al. (2002b), who ascribed the behavior to the competing effects of decreasing effective temperature and loss of cloud opacity.

We have also computed the EWs of a number of weaker atomic features, including the Na doublet at 2.207 μm, and a number of features from refractory elements, including Al, Mg, Fe, and Ca. Except for the Mg line at 1.183 μm, all of the features are a blend of a number of lines. Their EWs are tabulated in Table 9 and are shown as a function of spectral type in Figure 18. There is significant scatter, but all the lines weaken with increasing spectral type except for the Fe I line at 1.189 μm, which shows almost no correlation with spectral type. Additionally, all of the lines disappear by a spectral type of $\sim$L1 except for the Fe I line, which persists to $\sim$L5. The refractory element lines probably weaken in the late-type M dwarfs owing to the formation of condensates in the atmospheres of the dwarfs (Lodders 2002), but the effects of decreasing effective temperature may also play a role. Two stars, Gl 411 (M2 V) and Gl 213 (M4 V), have low Fe, Al, Na, and Ca EWs relative to the trend established by the other M dwarfs, suggesting that they may have low metallicities. The classification of Gl 213 as an old disk halo star by Leggett (1992) suggests that it may have a low metallicity, while the metallicity of Gl 411 has been measured to be [Fe/H] = -0.2 (Mould 1978). We will explore the variations in the EWs of these features more fully in a subsequent paper.

4. INDIVIDUAL OBJECTS OF INTEREST

4.1. *2MASS J2224−0158*

Object 2MASS J2224−0158 is classified as L4.5 based on its red-optical spectrum (Kirkpatrick et al. 2000). The 0.6–4.1 μm spectrum of 2MASS J2224−0158 is shown in Figure 19, along with the spectrum of 2MASS J1507−1627, a normal L5 dwarf. The two objects have the same spectral type within the errors ($\pm$0.5 subclass). The 2MASS J1507−1627 spectrum was scaled by the square of the ratio of the distances of the two objects to adjust its flux to the level that would be observed if it were at the distance of 2MASS J2224−0158. The spectrum of 2MASS J2224−0158 is depressed in the J and H bands relative to that of 2MASS J1507−1627, which results in a very red color $J - K =$ 2.051. The ^{12}CO 2–0 and 3–1 band heads at $\sim$2.3 μm in 2MASS J2224−0158 are also considerably deeper than in the spectrum of 2MASS J1507−1627.

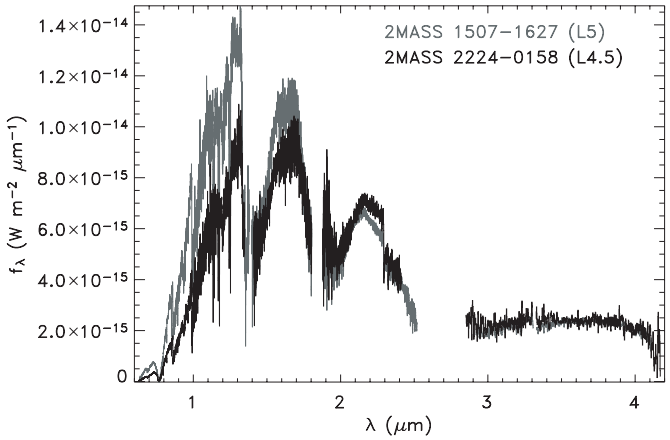

FIG. 19.—The 0.6–2.4 μm spectra of 2MASS J2224−0158 (L4.5) and 2MASS J1507−1627 (L5). The spectrum of 2MASS J1507−1627 has been scaled to appear as if the object were at the distance of 2MASS J2224−0158. The J- and H-band peaks of 2MASS J2224−0158 are suppressed relative to that of 2MASS J1507−1627, and the ^{12}CO band head in the spectrum of 2MASS J2224−0158 is considerably deeper than in the spectrum of 2MASS J1507−1627.

Interstellar extinction is probably not the cause of the extremely red color since 2MASS J2224−0158 lies at a distance of $\sim$11 pc. An examination of the blue POSS I plates also reveals no obvious extinction in the field of 2MASS J2224−0158. Therefore, the extremely red color of 2MASS J2224−0158 appears to be intrinsic to the object and may result from an unusually thick cloud deck, since dwarfs become progressively redder with an increasing column abundance of dust. The CO $\Delta\nu = +2$ band heads in the spectra of M giant stars are deeper than in the spectra of M dwarfs of the same spectral type (Kleinmann & Hall 1986). If this trend were to continue to cooler temperatures, the deep CO bands may indicate that 2MASS J2224−0158 has a low surface gravity.

4.2. *DENIS J0255−4700 and the L/T Transition*

There has been much interest in objects with spectral types at the transition between the L and T dwarfs (McLean et al. 2001; Nakajima et al. 2001; Schweitzer et al. 2002; Geballe et al. 2002; Burgasser et al. 2002b; Tsuji & Nakajima 2003). This interest stems from a desire not only to determine the exact spectral morphological changes that signal the transition to the T spectral class but also to understand why dwarfs at the L/T boundary (L7 to T3) have roughly the same effective temperature (Golimowski et al. 2004).

DENIS J0255−4700 was classified as bdL6 by Martín et al. (1999) and reclassified as $\sim$L8 by Kirkpatrick et al. (2000). Figure 20 shows the H-band spectra of DENIS J0255−4700 and SDSS J1254−0122 (T2) in the top panel and the K-band spectra of the same dwarfs in the bottom panel. In the H band, the $2\nu_3$ band of CH_4 at 1.67 μm is clearly present in the spectrum of DENIS J0255−4700. In addition, the broad absorption trough of the $2\nu_2 + \nu_3$ band centered at 1.63 μm, along with a number of individual CH_4 features (*dotted lines*), is also present in the spectrum of DENIS J0255−4700. The K-band spectrum of DENIS J0255−4700 also shows evidence of CH_4 absorption. There is an abrupt slope change in the K-band spectrum at $\sim$2.2 μm that is coincident with the absorption maximum of the $\nu_2 + \nu_3$ band. This feature has been seen in other late-type L

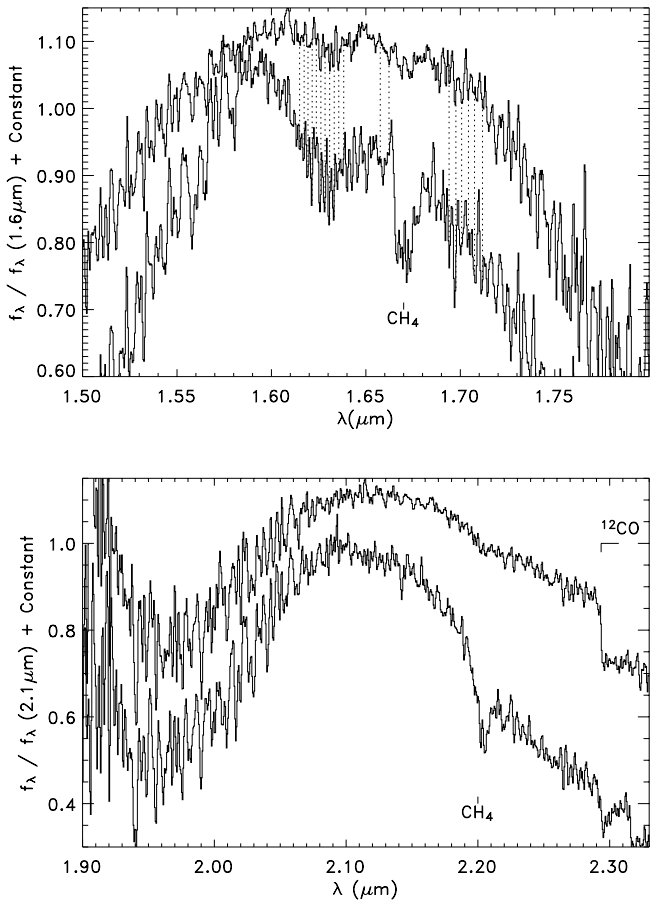

FIG. 20.—*H*- (*top*) and *K*-band (*bottom*) spectra of DENIS J0255−4700 (*upper spectrum*) and SDSS J1254−0122 (*lower spectrum*). The CH_4 features identified in the spectrum of the 2MASS J0559−1404 are indicated by dotted lines. Note that not all of the CH_4 lines identified in the spectrum of 2MASS J0559−1404 are present in the spectra of DENIS J0255−4700 and SDSS J1254−0122.

dwarfs, but there has been some disagreement about its carrier. For example, Tokunaga & Kobayashi (1999) ascribe a similar feature in the spectrum of DENIS J0205−11AB to collision-induced H_2 absorption. However, Nakajima et al. (2001) find evidence of CH_4 absorption in both *H*- and *K*-band spectra of 2MASS J0902+3517 (L6.5). Given the clear detection of CH_4 features in the *H* band, we also ascribe this feature in the spectrum of DENIS J0255−4700 to CH_4.

Given the detection of CH_4 absorption in the *H*- and *K*-band spectra of DENIS J0255−4700, should it be reclassified as a T dwarf? There are two spectral classification schemes currently in use for T dwarfs (Burgasser et al. 2002b; Geballe et al. 2002). The defining characteristic of a T dwarf given by Geballe et al. (2002) is "the appearance of methane absorption in the *H* band, i.e., to its earliest appearance in *both* the *H* and *K* bands." By this definition, DENIS J0255−4700 is a T dwarf. However, we have computed the spectral indices for DENIS J0255−4700 defined by Geballe et al. (2002) after smoothing the spectrum to $R \approx 500$ (the resolving power of the spectral standards). All of the Geballe et al. (2002) indices indicate that DENIS J0255−4700 has a spectral type earlier than T0. The discrepancy probably results from the difference in resolving power; the *H*-band methane features are simply too difficult to identify in the $R \approx 500$ spectrum. Therefore, in the Geballe et al. (2002) classification system, DENIS J0255−4700 should remain a late-type L dwarf.

Finally, Burgasser et al. (2002a) have suggested that late-type L and early-type T dwarfs may exhibit substantial photometric or spectroscopic variability due to the breakup of the cloud decks as they pass into the atmospheric convective zone. As DENIS J0255−4700 is the brightest ($K = 11.55$) late-type L dwarf, it would be an interesting target for both photometric and spectroscopic variability studies.

5. BOLOMETRIC FLUXES AND LUMINOSITIES

The effective temperatures of ultracool dwarfs are typically determined by combining observationally measured bolometric luminosities with theoretical stellar radii (e.g., Leggett et al. 1996, 2001, 2002; Dahn et al. 2002; Golimowski et al. 2004). The bolometric luminosities are measured using absolutely flux-calibrated 1–2.5 μm spectra, L'-band photometry to account for the flux emitted between 2.5 and 3.6 μm, and a Rayleigh-Jeans tail at $\lambda > 3.6$ μm. Although atmospheric models indicate that using L'-band photometry is a valid approximation, it has never been tested observationally. Our spectra are ideal for testing this assumption.

In order to construct spectra suitable for integration over all wavelengths, we follow the standard practice of extending the spectra shortward of 0.6 μm using published optical photometry and longward of 4.1 μm using a Rayleigh-Jeans tail (Berriman & Reid 1987; Leggett et al. 1996, 2001). The *U*, *B*, and *V* magnitudes of the M dwarfs (Leggett 1992) were converted to flux densities using the effective wavelength approach described by Leggett et al. (1996). For each dwarf spectrum, we linearly interpolated from zero flux at zero wavelength, through the *U*-, *B*-, and *V*-band flux densities if available, to the flux density at the bluest wavelength of the spectrum. The gaps in each spectrum at 1.85 and 2.6 μm were removed by linear interpolation between the flux densities at the gap edges. Finally, we extended a Rayleigh-Jeans tail from the reddest wavelength of each spectrum to infinity.

Since there are limited observations of ultracool dwarfs at $\lambda > 4$ μm, we must resort to model atmospheres to determine the validity of assuming a Rayleigh-Jeans tail at these wavelengths. We have compared the integrated flux of a Rayleigh-Jeans tail and the integrated flux of the NEXTGEN, DUSTY, and COND synthetic spectra (Allard et al. 2001) at various effective temperatures at $\lambda > 4.1$ μm. In gross terms, the NEXTGEN, DUSTY, and COND models are appropriate for M, L, and T dwarfs, respectively. The integrated flux of a Rayleigh-Jeans tail at $\lambda > 4.1$ μm agrees with that of the models to ~1%, ~5%, and ~20% for M, L, and T dwarfs, respectively. The large discrepancy between the Rayleigh-Jeans tail and the models appropriate for the T dwarfs (COND) is a result of absorption bands of H_2O, CH_4, and NH_3 in the 6–12 μm region (Roellig et al. 2004).

The integrated bolometric fluxes for the dwarfs with 0.6–4.1 μm spectra are listed in column (3) of Table 10. The errors in the bolometric fluxes include the error due to the photometry used to flux-calibrate the spectra and an estimate of the systematic error introduced by assuming a Rayleigh-Jeans tail at $\lambda > 4.1$ μm. Leggett et al. (1996, 2001, 2002) have computed bolometric fluxes for 11 of the M and L dwarfs in our sample. They compute these bolometric fluxes using near-infrared spectroscopy and L'-band photometry as described above. Their bolometric flux measurements agree with our measurements within the errors for all 11 of the dwarfs. This is not unexpected since the spectra are relatively featureless from 3.42 to 4.12 μm, the wavelengths at which the MKO-NIR L'-band filter transmission is 50% of the peak (Tokunaga et al. 2002). The good agreement between the two methods means that L'-band

TABLE 10
f_{bol} AND L_{bol} OF THE DWARFS

Object (1)	Spectral Type (2)	f_{bol} (W m^{-2}) (3)	m_{bol}[a] (4)	$\log_{10}(L_{bol}/L_{\odot})$[b] (5)	M_{bol} (6)
Gl 229A	M1 V	5.19E−11 ± 1.43E−12	6.72 ± 0.03	−1.27 ± 0.01	7.92 ± 0.03
Gl 411	M2 V	1.10E−10 ± 3.03E−12	5.91 ± 0.03	−1.66 ± 0.01	8.88 ± 0.03
Gl 388	M3 V	3.24E−11 ± 7.11E−13	7.24 ± 0.03	−1.62 ± 0.02	8.79 ± 0.04
Gl 213	M4 V	5.97E−12 ± 1.24E−13	9.07 ± 0.02	−2.21 ± 0.02	10.26 ± 0.05
Gl 51	M5 V	1.49E−12 ± 3.49E−14	10.58 ± 0.03	−2.30 ± 0.07	10.48 ± 0.17
Gl 406	M6 V	5.90E−12 ± 1.40E−13	9.08 ± 0.03	−2.98 ± 0.01	12.20 ± 0.03
vB 8	M7 V	4.73E−13 ± 1.18E−14	11.83 ± 0.03	−3.21 ± 0.01	12.77 ± 0.03
vB 10	M8 V	4.28E−13 ± 1.19E−14	11.93 ± 0.03	−3.34 ± 0.01	13.09 ± 0.03
LP 944−20	M9 V	2.02E−13 ± 4.67E−15	12.75 ± 0.03	−3.81 ± 0.02	14.27 ± 0.05
LHS 2924	M9 V	6.57E−14 ± 1.62E−15	13.97 ± 0.03	−3.62 ± 0.02	13.79 ± 0.04
BRI 0021−0214	M9.5 V	7.43E−14 ± 1.88E−15	13.84 ± 0.03	−3.51 ± 0.04	13.52 ± 0.10
2MASS J0746+2000AB	L0.5	8.07E−14 ± 2.09E−15	13.75 ± 0.03	−3.43 ± 0.01	13.31 ± 0.03
2MASS J1439+1929	L1	3.00E−14 ± 7.31E−16	14.82 ± 0.03	−3.72 ± 0.01	14.03 ± 0.03
Kelu-1	L2	2.02E−14 ± 5.09E−16	15.25 ± 0.03	−3.66 ± 0.03	13.89 ± 0.09
2MASS J1506+1321	L3	2.21E−14 ± 5.74E−16	15.15 ± 0.03	...	...
2MASS J0036+1821	L3.5	4.55E−14 ± 1.35E−15	14.37 ± 0.03	−3.97 ± 0.01	14.65 ± 0.04
2MASS J2224−0158	L4.5	1.58E−14 ± 4.84E−16	15.51 ± 0.03	−4.20 ± 0.01	15.24 ± 0.03
2MASS J1507−1627	L5	3.54E−14 ± 1.08E−15	14.64 ± 0.03	−4.16 ± 0.01	15.15 ± 0.03
SDSS J0539−0559	L5	1.20E−14 ± 3.79E−16	15.81 ± 0.03	−4.19 ± 0.03	15.22 ± 0.07
2MASS J0825+2115	L7	7.51E−15 ± 3.51E−16	16.32 ± 0.05	−4.58 ± 0.02	16.18 ± 0.05
DENIS J0255−4700	L8	3.15E−14 ± 1.46E−15	14.76 ± 0.05	...	...
SDSS J1254−0122	T2	4.82E−15 ± 3.30E−16	16.81 ± 0.07	−4.68 ± 0.04	16.45 ± 0.09
2MASS J0559−1404	T5	8.55E−15 ± 6.22E−16	16.18 ± 0.08	−4.56 ± 0.03	16.13 ± 0.08

[a] Here $m_{bol} = -2.5 \log f_{bol} - 18.988$ assuming $L_{\odot} = 3.86 \times 10^{26}$ W and $M_{bol_{\odot}} = +4.74$.
[b] Here $\log(L_{bol}/L_{\odot}) = \log f_{bol} - 2 \log \pi + 7.4913$ assuming $L_{\odot} = 3.86 \times 10^{26}$ W.

photometry can be used as a substitute for L-band spectroscopy, greatly simplifying the calculation of the bolometric fluxes of M and L dwarfs. The bolometric luminosities and absolute bolometric magnitudes of the dwarfs with measured parallaxes are also given in columns (5) and (6) of Table 10.

In principle, we could now use the derived bolometric luminosities to determine the effective temperatures of the dwarfs in our sample. However, since our L_{bol} measurements agree with those of Leggett et al. (2001), our T_{eff} estimates will also agree and therefore we do not repeat this analysis. We instead refer the reader to the recent work of Golimowski et al. (2004), who determined the effective temperatures of a large sample of ultracool dwarfs using the same technique as Leggett et al. (2001).

6. SUMMARY

We have presented a spectroscopic sequence of M, L, and T dwarfs, covering the wavelength range 0.6–4.1 μm, obtained with data from SpeX on the NASA IRTF, the IRCS on the Subaru telescope, and previously published red-optical spectra. Neutral lines of Al, Fe, Mg, Ca, and Ti are identified in the spectra of the M dwarfs but are all but absent in the spectra of the L dwarfs. Nineteen new weak CH_4 absorption features are identified in the H-band spectrum of 2MASS J0559−1404. We also confirm the presence of the 0–0 band of the $A\ ^4\Pi$–$X\ ^4\Sigma^-$ transition of VO at ~1.06 μm in the spectra of late-type M dwarfs and detect it for the first time in the spectra of the early-type L dwarfs. No absorption features of Cs, Rb, or CrH, hallmarks of L dwarf spectra in the red-optical, are found at $\lambda > 1.0$ μm. The suite of spectroscopic indices derived by McLean et al. (2003) generally saturate for spectral types earlier than ~M4 V, thus limiting their usefulness to later spectral types. The bolometric luminosities of the dwarfs in our sample agree with previously published results that make use of L'-band photometry rather than spectroscopy. This result validates the use of L'-band photometry as a substitute for spectroscopy. Finally, 2MASS J2224−0158 (L4.5) has a very red near-infrared spectrum and deep CO bands that may be indicative of low surface gravity and unusually thick condensate clouds. The SpeX spectra can be obtained at the SpeX Web site,[9] and the 0.6–4.1 μm spectra are available on request from the first author.

The authors wish to thank Davy Kirkpatrick, Sandy Leggett, Adam Burgasser, Hugh Jones, Eduardo Martín, Tod Henry, and the RECONS team for providing the M, L, and T dwarf optical spectra, Sumner Davis and Ray Nassar for their high-resolution emission spectra of VO and CH_4, and Mark Marley and Richard Freedman for useful discussions. We also thank the anonymous referee for his/her prompt review of the manuscript. This publication makes use of data from the Two Micron All Sky Survey, which is a joint project of the University of Massachusetts and the Infrared Processing and Analysis Center and funded by the National Aeronautics and Space Administration and the National Science Foundation. This research has made use of the SIMBAD database, operated at CDS, Strasbourg, France. M. C. C. acknowledges financial support from the NASA Infrared Telescope Facility and NASA through the *Spitzer Space Telescope* Fellowship Program.

[9] See http://irtfweb.ifa.hawaii.edu/Facility/spex.

REFERENCES

Ali, B., Carr, J. S., Depoy, D. L., Frogel, J. A., & Sellgren, K. 1995, AJ, 110, 2415
Allard, F., Hauschildt, P. H., Alexander, D. R., Tamanai, A., & Schweitzer, A. 2001, ApJ, 556, 357
Allard, F., Hauschildt, P. H., & Schwenke, D. 2000, ApJ, 540, 1005
Auman, J. J. 1967, ApJS, 14, 171
Basri, G., Marcy, G. W., & Graham, J. R. 1996, ApJ, 458, 600
Berriman, G., & Reid, N. 1987, MNRAS, 227, 315
Borysow, A. 2002, A&A, 390, 779
Borysow, A., Jorgensen, U. G., & Zheng, C. 1997, A&A, 324, 185
Burgasser, A. J. 2001, Ph.D. thesis, Caltech
Burgasser, A. J., Kirkpatrick, J. D., Liebert, J., & Burrows, A. 2003, ApJ, 594, 510
Burgasser, A. J., Marley, M. S., Ackerman, A. S., Saumon, D., Lodders, K., Dahn, C. C., Harris, H. C., & Kirkpatrick, J. D. 2002a, ApJ, 571, L151
Burgasser, A. J., et al. 2000, AJ, 120, 1100
———. 2002b, ApJ, 564, 421
Burrows, A., Ram, R. S., Bernath, P., Sharp, C. M., & Milsom, J. A. 2002, ApJ, 577, 986
Buser, R., & Kurucz, R. L. 1992, A&A, 264, 557
Chueng, A. S., Taylor, A. W., & Merer, A. J. 1982, J. Mol. Spectrosc., 92, 391
Cohen, M., Wheaton, W. A., & Megeath, S. T. 2003, AJ, 126, 1090
Cushing, M. C., Rayner, J. T., Davis, S. P., & Vacca, W. D. 2003, ApJ, 582, 1066
Cushing, M. C., Vacca, W. D., & Rayner, J. T. 2004, PASP, 116, 362
Dahn, C. C., et al. 2002, AJ, 124, 1170
Danielson, R. E. 1966, ApJ, 143, 949
Dulick, M., Bauschlicher, C. W., Burrows, A., Sharp, C. M., Ram, R. S., & Bernath, P. 2003, ApJ, 594, 651
Epchtein, N., et al. 1997, Messenger, 87, 27
Fan, X., et al. 2000, AJ, 119, 928
Fisher, R. A., Knopf, W. C., & Eshbach Kinney, F. 1959, ApJ, 130, 683
Galehouse, D. C., Davis, S. P., & Brault, J. W. 1980, ApJS, 42, 241
Geballe, T. R., et al. 2002, ApJ, 564, 466
Gizis, J. E., Monet, D. G., Reid, I. N., Kirkpatrick, J. D., Liebert, J., & Williams, R. J. 2000, AJ, 120, 1085
Golimowski, D. A., et al. 2004, AJ, 127, 3516
Goorvitch, D. 1994, ApJS, 95, 535
Hinkle, K., Wallace, L., & Livingston, W. 1995, PASP, 107, 1042
Jones, H. R. A., Longmore, A. J., Allard, F., Hauschildt, P. H., Miller, S., & Tennyson, J. 1995, MNRAS, 277, 767
Jones, H. R. A., Longmore, A. J., Jameson, R. F., & Mountain, C. M. 1994, MNRAS, 267, 413
Jones, H. R. A., Pavlenko, Y., Viti, S., & Tennyson, J. 2002, MNRAS, 330, 675
Joyce, R. R., Hinkle, K. H., Wallace, L., Dulick, M., & Lambert, D. L. 1998, AJ, 116, 2520
Kirkpatrick, J. D., Allard, F., Bida, T., Zuckerman, B., Becklin, E. E., Chabrier, G., & Baraffe, I. 1999a, ApJ, 519, 834
Kirkpatrick, J. D., Henry, T. J., & McCarthy, D. W. 1991, ApJS, 77, 417
Kirkpatrick, J. D., Henry, T. J., & Simons, D. A. 1995, AJ, 109, 797
Kirkpatrick, J. D., Kelly, D. M., Rieke, G. H., Liebert, J., Allard, F., & Wehrse, R. 1993, ApJ, 402, 643
Kirkpatrick, J. D., et al. 1999b, ApJ, 519, 802
———. 2000, AJ, 120, 447
Kleinmann, S. G., & Hall, D. N. B. 1986, ApJS, 62, 501
Kobayashi, N., et al. 2000, Proc. SPIE, 4008, 1056
Koornneef, J., Bohlin, R., Buser, R., Horne, K., & Turnshek, D. 1986, Highlights Astron., 7, 833
Leggett, S. K. 1992, ApJS, 82, 351
Leggett, S. K., Allard, F., Berriman, G., Dahn, C. C., & Hauschildt, P. H. 1996, ApJS, 104, 117
Leggett, S. K., Allard, F., Geballe, T. R., Hauschildt, P. H., & Schweitzer, A. 2001, ApJ, 548, 908
Leggett, S. K., Allard, F., & Hauschildt, P. H. 1998, ApJ, 509, 836
Leggett, S. K., et al. 2000, ApJ, 536, L35
———. 2002, ApJ, 564, 452
Lodders, K. 1999, ApJ, 519, 793
Lodders, K. 2002, ApJ, 577, 974
Martín, E. L., Delfosse, X., Basri, G., Goldman, B., Forveille, T., & Zapatero Osorio, M. R. 1999, AJ, 118, 2466
McGovern, M. R., Kirkpatrick, J. D., McLean, I. S., Burgasser, A. J., Prato, L., & Lowrance, P. J. 2004, ApJ, 600, 1020
McLean, I. S., McGovern, M. R., Burgasser, A. J., Kirkpatrick, J. D., Prato, L., & Kim, S. S. 2003, ApJ, 596, 561
McLean, I. S., Prato, L., Kim, S. S., Wilcox, M. K., Kirkpatrick, J. D., & Burgasser, A. 2001, ApJ, 561, L115
McLean, I. S., et al. 2000, ApJ, 533, L45
Mégessier, C. 1995, A&A, 296, 771
Meyer, M. R., Edwards, S., Hinkle, K. H., & Strom, S. E. 1998, ApJ, 508, 397
Monet, D. G., Dahn, C. C., Vrba, F. J., Harris, H. C., Pier, J. R., Luginbuhl, C. B., & Ables, H. D. 1992, AJ, 103, 638
Mould, J. R. 1978, ApJ, 226, 923
Nakajima, T., Oppenheimer, B. R., Kulkarni, S. R., Golimowski, D. A., Matthews, K., & Durrance, S. T. 1995, Nature, 378, 463
Nakajima, T., Tsuji, T., & Yanagisawa, K. 2001, ApJ, 561, L119
Nassar, R., & Bernath, P. 2003, J. Quant. Spectrosc. Radiat. Transfer, 82, 279
Noll, K. S., Geballe, T. R., Leggett, S. K., & Marley, M. S. 2000, ApJ, 541, L75
Noll, K. S., Geballe, T. R., & Marley, M. S. 1997, ApJ, 489, L87
Oppenheimer, B. R., Kulkarni, S. R., Matthews, K., & van Kerkwijk, M. H. 1998, ApJ, 502, 932
Perryman, M. A. C., et al. 1997, A&A, 323, L49
Phillips, J. G., Davis, S. P., Lindgren, B., & Balfour, W. J. 1987, ApJS, 65, 721
Press, W. H., Teukolsky, S. A., Vetterling, W. T., & Flannery, B. P. 1992, Numerical Recipes in FORTRAN: The Art of Scientific Computing (2nd ed.; Cambridge: Cambridge Univ. Press)
Rayner, J. T., Toomey, D. W., Onaka, P. M., Denault, A. J., Stahlberger, W. E., Vacca, W. D., Cushing, M. C., & Wang, S. 2003, PASP, 115, 362
Rebolo, R., Martin, E. L., Basri, G., Marcy, G. W., & Zapatero-Osorio, M. R. 1996, ApJ, 469, L53
Reid, I. N., Burgasser, A. J., Cruz, K. L., Kirkpatrick, J. D., & Gizis, J. E. 2001, AJ, 121, 1710
Reid, I. N., Kirkpatrick, J. D., Gizis, J. E., Dahn, C. C., Monet, D. G., Williams, R. J., Liebert, J., & Burgasser, A. J. 2000, AJ, 119, 369
Roellig, T. L., et al. 2004, ApJS, 154, 418
Ruiz, M. T., Leggett, S. K., & Allard, F. 1997, ApJ, 491, L107
Saumon, D., Geballe, T. R., Leggett, S. K., Marley, M. S., Freedman, R. S., Lodders, K., Fegley, B., & Sengupta, S. K. 2000, ApJ, 541, 374
Saumon, D., Marley, M. S., & Lodders, K. 2003a, preprint (astro-ph/0310805)
Saumon, D., Marley, M. S., Lodders, K., & Freedman, R. S. 2003b, in IAU Symp. 211, Brown Dwarfs, ed. E. Martín (San Francisco: ASP), 345
Schweitzer, A., Gizis, J. E., Hauschildt, P. H., Allard, F., Howard, E. M., & Kirkpatrick, J. D. 2002, ApJ, 566, 435
Sembach, K. R., & Savage, B. D. 1992, ApJS, 83, 147
Skrutskie, M. F., et al. 1997, in The Impact of Large Scale Near-IR Sky Surveys, ed F. Garzón et al. (Dordrecht: Kluwer), 25
Testi, L., et al. 2001, ApJ, 552, L147
Tinney, C. G., & Reid, I. N. 1998, MNRAS, 301, 1031
Tinney, C. G., Reid, I. N., Gizis, J., & Mould, J. R. 1995, AJ, 110, 3014
Tokunaga, A. T. 2000, in Allen's Astrophysical Quantities, ed. A. N. Cox (4th ed.; New York: Springer), 151
Tokunaga, A. T., & Kobayashi, N. 1999, AJ, 117, 1010
Tokunaga, A. T., Simons, D. A., & Vacca, W. D. 2002, PASP, 114, 180
Tsuji, T., & Nakajima, T. 2003, ApJ, 585, L151
Vacca, W. D., Cushing, M. C., & Rayner, J. T. 2003, PASP, 115, 389
van Altena, W. F., Lee, J. T., & Hoffleit, E. D. 1995, The General Catalogue of Trigonometric [Stellar] Parallaxes (4th ed.; New Haven: Yale Univ. Obs.)
Vrba, F. J., et al. 2004, AJ, 127, 2948
Wallace, L., & Hinkle, K. 2001, ApJ, 559, 424
———. 2002, AJ, 124, 3393
Wilson, J. C., et al. 2003, in IAU Symp. 211, Brown Dwarfs, ed. E. Martín (San Francisco: ASP), 197
York, D. G., et al. 2000, AJ, 120, 1579